2016

INVESTIGATION OF THE RESISTANCE TO DEMAGNETIZATION IN BULK RARE-EARTH MAGNETS COMPRISED OF CRYSTALLOGRAPHICALLY-ALIGNED, SINGLE-DOMAIN CRYSTALLITES WITH MODIFIED INTERGRANULAR PHASE

Jie Li
Michigan Technological University, jli10@mtu.edu

INVESTIGATION OF THE RESISTANCE TO DEMAGNETIZATION IN BULK RARE-EARTH MAGNETS COMPRISED OF CRYSTALLOGRAPHICALLY-ALIGNED, SINGLE-DOMAIN CRYSTALLITES WITH MODIFIED INTERGRANULAR PHASE

By

Jie Li

A DISSERTATION

Submitted in partial fulfillment of the requirements for the degree of

DOCTOR OF PHILOSOPHY

In Engineering Physics

MICHIGAN TECHNOLOGICAL UNIVERSITY

2016

This dissertation has been approved in partial fulfillment of the requirements for the Degree of DOCTOR OF PHILOSOPHY in Engineering Physics.

Department of Physics

Dissertation Advisor: *Peter D. Moran*

Committee Member: *Ravindra Pandey*

Committee Member: *Stephen Hackney*

Committee Member: *Stephen Kampe*

Committee Member: *Yongmei Jin*

Department Chair: *Ravindra Pandey*

Content

List of Tables

List of Figures

Acknowledgements

I would like to express my deepest gratitude for my advisor, Dr. Peter Moran, for all the help and guidance he has given me over the last 5 years. From the very beginning he went out of his way to find me this research project, and he has continued to ensure that I have funding to complete what has been an amazing journey. He showed me how to do research and encouraged me to keep going in times when everything seemed to be going wrong.

I would like to thank Dr. Stephen Hackney, who has always been patient in answering my many questions and willing to help me acquire wonderful SEM images. I would also like to thank Yucong Wang from the GM Company, for offering guidance to the project, and Dr. Frederick Pinkerton from the GM Company, for running all of my VSM experimentation.

I would like to thank my committee members, Dr. Ravindra Pandey, Dr. Stephen Kampe, and Dr. Yongmei Jin, for reviewing my paper and giving me invaluable suggestions for future work.

I would like to thank the faculty and staff of the Physics and Materials Science and Engineering Departments at Michigan Tech, for their support and their friendship. I would especially like to thank Paul Fraley, for being a great help in all things related to experimentation. From training me in operation of the melt spinner to repairing the hot press, he has always been happy to help any way he can and quick to offer advice.

I would like to thank my coworker Li Chen, who spent many long hours with me during experimentation, and who was always a wonderful friend and there to brainstorm solutions to problems in research. I would also like to thank Helen Rau and Karl Warsinski for all their time spent cutting my samples with the EDM.

I would like to thank my parents for being supportive of me and for visiting me when I was unable to go back to China. I would also like to thank all my friends for their support, especially my ex-roommate, Dan Yi, who was amazing and cleaned the apartment and cooked me food when I was too busy doing experiments.

Lastly I would like to thank my awesome fiancé, Kyle Deane, for always being there to support me and make me laugh. This last summer has been the most wonderful summer of my life, full of fishing, berry picking, northern lights, and agate hunting, and the challenge of finishing up my degree has seemed much less daunting with his help. I really don't know how I could have gotten to this point without him.

Abstract

The research presented in this dissertation investigates whether an increased coercivity of Neodymium-Iron-Boron ($Nd_2Fe_{14}B$) based bulk magnets at elevated temperature (160°C), which is now only obtainable by substituting ~7wt% dysprosium (Dy) for a portion of neodymium (Nd), can be achieved through specific microstructural modifications with decreased Dy concentrations. The approach is to reduce the size of individual crystallographically-aligned grains in the magnet so that each grain can only support a single magnetic domain and to simultaneously dilute the Nd-Fe inter-granular phase present in conventional magnets with a non-Fe-containing, Nd-rich phase (Nd-Cu alloy) in an attempt to partially magnetically isolate the individual crystallites. The results of this research show that hot-deformed bulk magnets with the microstructural features described above have similar coercivity to commercially sintered magnets that are used in traction motor of electric and hybrid vehicles. The increase in coercivity due to the modification of intergranular phase is analyzed in the framework of what would be expected from the partially magnetic isolation of the individual grains.

Chapter 1

Introduction

1.1 Research Goal

The overall goal of this research is to determine whether the coercivity of bulk rare-earth magnets could approach the maximum value possible for $RE_2TM_{14}B$ (Rear Earth-Transaction Metal-Boron), if the rare-earth bulk magnets are comprised of crystallographically-aligned, submicron ($RE_2TM_{14}B$) grains and the original Fe-containing Nd-rich intergranular phase is diluted by other non-ferromagnetic phase. In such a case, each grain would only support a single magnetic domain, and would be partially magnetically isolated from neighboring grains. The coercivity would then be large enough to eliminate the need for dysprosium (Dy) in the magnets used in traction motors of electric and hybrid vehicles. There are several tasks that must be performed to satisfy the overall research goal.

1. Determine the minimum amount of dysprosium needed in $Nd_2Fe_{14}B$-based magnets to operate in transaction motors of hybrid and electric vehicles based on currently commercial manufacturing processes.
2. Determine the impact of hot-deformation parameters on the microstructural and magnetic properties of magnets.
3. Determine whether it is possible to produce hot-deformed bulk magnets that are comprised of crystallographically-aligned, submicron $Nd_2Fe_{14}B$ grains when the inter-granular phase is diluted by non-ferromagnetic Nd-rich phase.
4. Determine whether the developed hot-deformed magnets whose microstructure is dramatically different from that of commercial sintered magnets can still satisfy the requirement for transaction motors used in hybrid and electric vehicles but with less amount of dysprosium.
5. Analyze the physical mechanism behind the phenomena that the coercivity is increased by modifying the inter-granular phase with a non-ferromagnetic phase.

1.2 Motivations for Research

The technological motivation for this research is to reduce the amount of Dy needed in magnets used for traction motors of electric and hybrid vehicles. About 4.5 million hybrid and electric vehicles were sold worldwide in 2012, and each requires ~1kg of $Nd_2Fe_{14}B$-based permanent magnets. Dy, substituted for some of the neodymium in $Nd_2Fe_{14}B$ magnets to retain high coercivity ($\mu_0 H_C$) at elevated temperature (~160°C), is more expensive than Nd. In commercially manufactured sintered $Nd_2Fe_{14}B$-based magnets,

~7weight percent of Dy is added to increase the coercivity up to ~0.9T (the required value for traction motors) at 160°C. This increases the cost of the materials from ~$35/kg to ~$140/kg. The high price and low availability of Dy lead to a large and growing demand among auto manufacturers for magnets with less or no Dy that exhibit sufficient coercivity and remanence (Br).

The scientific motivation for the proposed research is to improve our current understanding of demagnetization physics in these bulk rare-earth magnets, and to improve our understanding of the selective dissolution and re-precipitation phenomena operating during the hot deformation process to make $Nd_2Fe_{14}B$-based magnets. Though there are bulk rare-earth magnets reported recently that have increased coercivity after the non-magnetic Nd-rich phase diffusion process, the amount or Nd-rich phase is significantly larger than that used in the process reported in this research and the physical mechanism behind the phenomena is poorly understood. The work in this research produces $Nd_2Fe_{14}B$-based magnets by a more simplified approach and analyzes the microstructural properties and demagnetization curves of those magnets in the framework of a phenomenological model and stray field theory. This information will be a significant addition to the scientific body of knowledge.

1.3 Organization of the Dissertation

The following chapters will first give the reader a general background in the intrinsic magnetic properties of bulk $Nd_2Fe_{14}B$-based magnets, general demagnetization physics

and a brief description of current commercial manufacturing processes and hot-deformation process. A phenomenological model used to analyze the effect of microstructural properties on coercivity of magnetic materials will be introduced. Secondly, the experimental techniques used in this research to characterize the microstructural and magnetic properties of materials will be described. Thirdly, the minimum amount of Dy currently needed in $RE_2TM_{14}B$ magnets to operate in the transaction motors of hybrid and electric vehicles will be determined. Fourthly, the optimal parameters for hot-deformation process that produces bulk magnets with crystallographically-aligned submicron crystallites by means of a selective dissolution and re-precipitation mechanism will be determined. Finally, the effect of diluting the inter-granular phase by adding non-ferromagnetic Nd-rich phase on the magnetic properties of materials and the physics mechanism behind this phenomena will be discussed.

Chapter 2

Background

In this chapter, the physics background of magnetic materials will be introduced. The effects of chemical composition and microstructural properties on the magnetic performance of $Nd_2Fe_{14}B$-based permanent magnets will be discussed. Two major processes to manufacture bulk $Nd_2Fe_{14}B$-based permanent magnets will be introduced and the differences in microstructural properties of these bulk magnets will be compared. A phenomenological model used to analyze the effect of microstructural properties on coercivity of magnetic materials will be introduced.

2.1 Intrinsic Magnetic Properties

Saturation magnetization (M_S), magnetocrystalline anisotropy (K_1), and the exchange constant (A) are three intrinsic magnetic properties of permanent magnetic materials. Magnetization is the vector sum of atomic magnetic moments per unit volume. When an

external magnetic field is applied to a magnet, the atomic magnetic moments inside the magnet rotate to align with the external field to reduce the magnetostatic energy. This increases the magnetization of the magnet in the direction of the externally applied field. If this external field is large enough, the magnetization of the material becomes saturated and does not increase with the increasing external magnetic field. This maximum value is called the saturation magnetization (M_S). At saturation, all of the magnetic moments are mutually aligned along the external field.

If the magnetic properties of a material vary with the directions in which they are measured, this magnetic material is considered to be magnetically anisotropic. Magnetocrystalline anisotropy is an intrinsic property of a material. Anisotropic magnetic materials have a magnetocrystalline easy direction(s) and a magnetocrystalline hard direction(s). The magnetocrystalline easy and hard directions represent the energetically favorable and unfavorable directions of spontaneous magnetization, respectively. These directions are determined by the specific crystal structure of the material and the interactions between the atomic moments of the atoms in the crystal structure. The physical origin of magnetocrystalline anisotropy is the spin-orbital coupling, and the strength of it is represented by the anisotropy constant, K_1. Since K_1 only depends on the crystal structure and the atoms in the crystal structure, it is not sensitive to the microstructure of the material.

The crystal anisotropy field (H_K) is a virtual field that would have to be applied parallel to the hard direction to demagnetize a single domain particle by rotating the M_S vector against the crystallographic anisotropy that tends to keep it oriented in the magnetocrystalline easy

direction. This anisotropy field is expressed in terms of M_S and K_1 by the following equation:

$$H_K = \frac{2K_1}{M_S} \tag{2.1}$$

Exchange energy, E_{ex}, which describes the exchange coupling between two adjacent atoms is responsible for ferromagnetism.

$$E_{ex} = -2JS^2 \cos\varphi_{ij} \tag{2.2}$$

J is the exchange integral and represents the exchange effect. φ_{ij} is the angle between the two adjacent atoms with same spin S. In ferromagnetic materials ($J > 0$), when the two neighboring atomic magnetic moments are aligned parallel, the exchange energy decreases to the minimum. The exchange constant (A) is used when the exchange energy is expressed in a continuum form.

$$E_{ex} = -2A\cos(\frac{d\varphi}{dx}) \tag{2.3}$$

2.2 Effect of Chemical Compositions on M_S and H_K

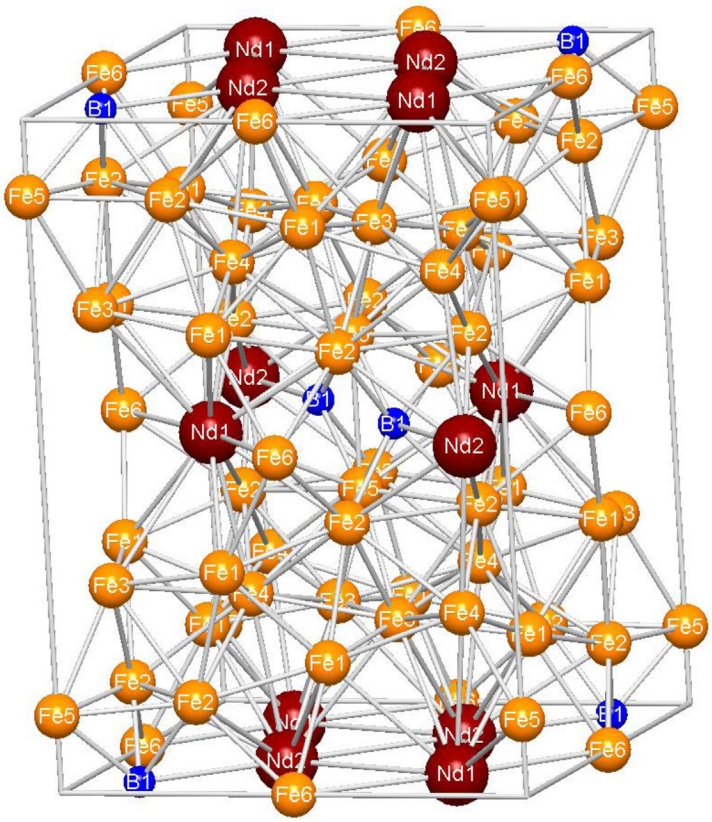

Figure 2-1 The tetragonal unit cell of the $Nd_2Fe_{14}B$ crystal structure, image created with Pearson's Crystal Data software using a crystallography data base[1].

Both saturation magnetization (M_S) and the crystal anisotropy field (H_K) are sensitive to the chemical compositions of the materials. The extension of Vegard's law is used to estimate the effect of chemical compositions on changing M_S and H_K of magnetic materials. Figure 2-1 displays the tetragonal unit cell of an $Nd_2Fe_{14}B$ crystal structure. Many other elements can replace the Nd, Fe, and B of an $Nd_2Fe_{14}B$ compound without changing the crystal structure. Different substitutive elements have different impacts on the magnetic

properties. For example, if Dy is substituted for some of the Nd in an $Nd_2Fe_{14}B$ material, M_S will decrease and H_K will increase. The reason for the decrease in M_S is that Nd and Fe magnetic moments are coupled ferromagnetically, while Dy and Fe magnetic moments are coupled antiferromagnetically[2]. The increase in H_K is due to the larger value of H_K in $Dy_2Fe_{14}B$ as compared to $Nd_2Fe_{14}B$. It has been shown that M_S and H_K of $[Dy_xNd_{1-x}]_2Fe_{14}B$ vary linearly with "x" between the values of M_S and H_K for the end compounds $Nd_2Fe_{14}B$ and $Dy_2Fe_{14}B$; M_S and H_K of $Nd_2[Fe_mCo_{1-m}]_{14}B$ vary linearly with "m" between the values of M_S and H_K for the end compounds $Nd_2Fe_{14}B$ and $Nd_2Co_{14}B$[3, 4]. Then, the saturation magnetization and anisotropy field of $[Dy_xPr_yNd_{1-x-y}]_2[Fe_{1-m}Co_m]_{14}$ materials can be estimated by applying Vegard's law to the M_S and H_K of the end compounds $RE_2Fe_{14}B$ (RE=Nd, Pr, Dy). The relationships are shown in Equation (2.4) and (2.5).

$$\begin{aligned} M_{S[Dy_x Pr_y Nd_{1-x-y}]_2[Fe_{1-m}Co_m]_{14}B} &= M_{S[Nd_2Fe_{14}B]} + x\times(M_{S[Dy_2Fe_{14}B]} - M_{S[Nd_2Fe_{14}B]}) \\ &\quad + y\times(M_{S[Pr_2Fe_{14}B]} - M_{S[Nd_2Fe_{14}B]}) \\ &\quad + m\times(M_{S[Nd_2Co_{14}B]} - M_{S[Nd_2Fe_{14}B]}) \end{aligned} \tag{2.4}$$

$$\begin{aligned} H_{K[Dy_x Pr_y Nd_{1-x-y}]_2[Fe_{1-m}Co_m]_{14}B} &= H_{K[Nd_2Fe_{14}B]} + x\times(H_{K[Dy_2Fe_{14}B]} - H_{K[Nd_2Fe_{14}B]}) \\ &\quad + y\times(H_{K[Pr_2Fe_{14}B]} - H_{K[Nd_2Fe_{14}B]}) \\ &\quad + m\times(H_{K[Nd_2Co_{14}B]} - H_{K[Nd_2Fe_{14}B]}) \end{aligned} \tag{2.5}$$

The effect of Co substituted for some of the Fe on varying M_S and H_K can be calculated by:

$$m\times(M_{S[Nd_2Co_{14}B]} - M_{S[Nd_2Fe_{14}B]}) = M_{S[Nd_2[Fe_{1-m}Co_m]_{14}B]} - M_{S[Nd_2Fe_{14}B]} \tag{2.6}$$

$$m\times(H_{K[Nd_2Co_{14}B]} - H_{K[Nd_2Fe_{14}B]}) = H_{K[Nd_2[Fe_{1-m}Co_m]_{14}B]} - H_{K[Nd_2Fe_{14}B]} \tag{2.7}$$

Figure 2-2 shows the temperature dependence of M_S and H_K for the end compounds $RE_2Fe_{14}B$ (RE=Dy, Nd, Pr) obtained from literature[5]. The temperature dependence of

M_S and H_K of $Nd_2[Fe_{1-m}Co_m]_{14}B$ material are gathered from Matsuura's experimental results[6], which are illustrated in Figure 2-3.

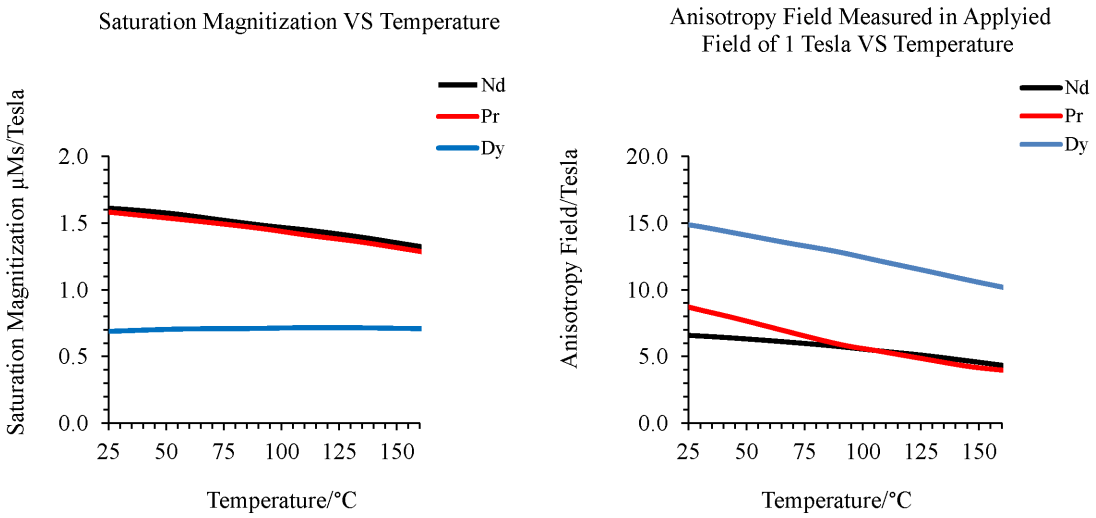

Figure 2-2 Saturation magnetization and anisotropy field of pure $RE_2Fe_{14}B$ magnet as a function of temperature.[5]

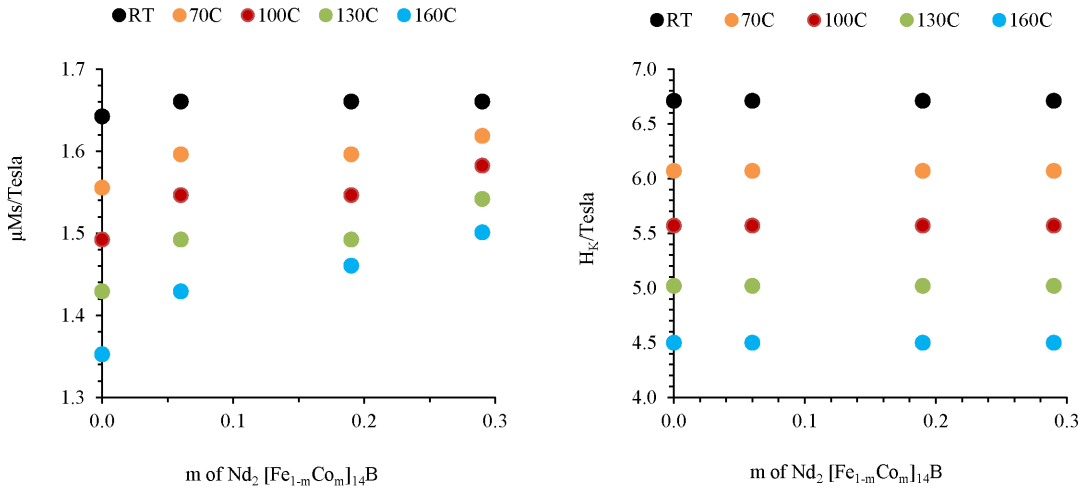

Figure 2-3 Saturation magnetization and anisotropy field of $Nd_2[Fe_{1-m}Co_m]_{14}B$ at different temperatures.[6]

2.3 Effect of Volume Percent of Hard Phase on M_S and H_K

In addition to chemical compositions, M_S and H_K also depends on the volume percent of effective magnetic hard phase. The $RE_2TM_{14}B$ phase is called magnetic hard phase and the secondary phase surrounds the grains is called intergranular phase. Usually bulk magnets consist of both effective magnetic hard phase and also intergranular phases. A low melting point RE-rich eutectic phase is found along grain boundaries and at the triple junctions[7] of $RE_2TM_{14}B$ materials. This intergranular phase allows the process to result in a fully-dense bulk magnet but will lower the saturation magnetization by decreasing the volume percent of effective $RE_2TM_{14}B$ phase. The volume percent of hard phase can be calculated based on the stoichiometry of the magnet and the phase diagram. As a result, the overall saturation magnetization and anisotropy field can be expressed as:

$$M_{Soverall} = Vol\%_{[RE_2TM_{14}B]} \cdot M_{S[RE_2TM_{14}B]} \tag{2.8}$$

$$H_{K,overall} = Vol\%_{[RE_2TM_{14}B]} \cdot H_{K[RE_2TM_{14}B]} \tag{2.9}$$

where $Vol\%_{[RE_2TM_{14}B]}$ is the volume percent of magnetic hard phase.

2.4 Demagnetization Curves and the Definition of Coercivity and Remanence

Coercivity and remanence are two of the most important quantities characterizing the magnetic performance of a permanent magnet. For a ferromagnetic material, when the external field is removed, the magnetization of the material decreases to a large fraction of M_S, which is called the remanence. The remanence represents the maximum flux projected

by the magnet under operating conditions. Coercivity is a measure of the reverse field under which the magnets become fully demagnetized. These values can be obtained from the demagnetization curve, which is the second quadrant of the hysteresis loop (shown in Figure 2-4). The intersection of a demagnetization curve with the vertical axis is the remanence, and the intersection of the demagnetization curve with the horizontal axis is the coercivity. Both coercivity and remanence decrease as temperature increases. This is because the increase in temperature leads to an increase in the amplitude of the thermally induced deviations of the atomic magnetic moments in the material. As a result, the magnetic dipole moments will be less aligned at higher temperatures than at the lower temperatures. Both the coercivity and remanence of a specific material are determined by two intrinsic magnetic properties, the saturation magnetization (M_S) and anisotropy field (H_K). Larger saturation magnetization and anisotropy field typically results in larger remanence and coercivity. Other than M_S and H_K, remanence and coercivity are also influenced by the microstructural properties of materials. The effect of microstructural properties on remanence and coercivity are discussed in the following section.

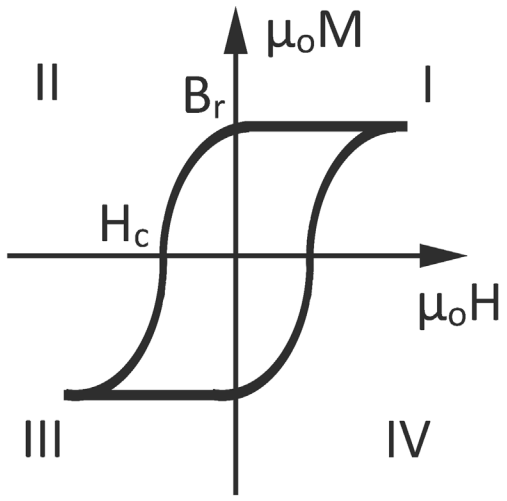

Figure 2-4 A typical hysteresis loop of a permanent magnet.

2.5 Effect of Microstructure on H_C and B_r

The remanence of bulk $Nd_2Fe_{14}B$ magnets is an appreciable fraction (70%-85%) of M_S [8-10]. In contrast, experimentally observed coercivity of a bulk material is only a small fraction of the anisotropy field. In general H_C/H_K ratio in conventionally manufactured magnets is on the order of ~0.1 or ~0.2. This is due to the microstructural properties of materials. Bulk $Nd_2Fe_{14}B$ magnets are polycrystalline materials which consist of many crystallites of varying size and orientation. Each crystallite is surrounded by the inter-granular phase. The size of crystallites and chemical compositions of the inter-granular phase affect the remanence and coercivity.

2.5.1 Magnetic Domain

Magnetic domains are the regions in which all of the magnetic moments of atoms are aligned in the same direction. For $Nd_2Fe_{14}B$ single domain particles with uniaxial anisotropy, their easy directions are [001] or $[00\bar{1}]$. The magnetization of a single domain is equal to the saturation magnetization, M_S. The overall magnetization of the bulk magnet is equal to the vector sum of magnetization of the individual magnetic domains. Typically, there will exist multiple magnetic domains in a single crystalline volume, resulting in a lower overall magnetization and reducing the volumetric magnetostatic energy of the body, shown in Figure 2-5. Each domain is separated from the others by a domain wall, a region where the orientation of the magnetization rotates by 180° over a small distance. The increase in potential energy per area of domain wall due to the presence of this domain wall is offset by the decrease in magnetostatic energy resulting from a body consisting of multiple domains.

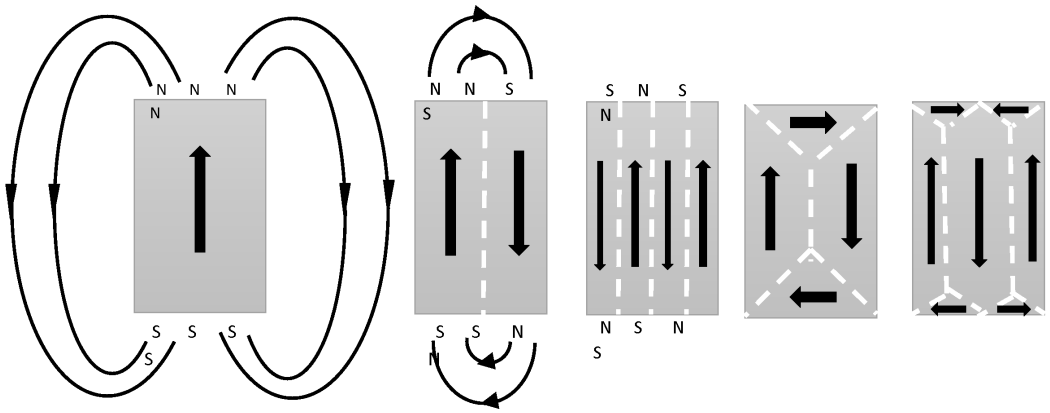

Figure 2-5 The formation of magnetic domains.

There exists a critical size below which a crystallite will not split into multiple smaller domains. This is because the reduction of the magnetostatic energy resulting from splitting into two domains cannot offset the energy of the domain wall between these two domains. The critical diameter for a spherical crystallite can be expressed in terms of M_S, K_1 and A:

$$d_c \approx 70\frac{\sqrt{AK_1}}{\mu_0 M_S{}^2} \tag{2.10}$$

For $Nd_2Fe_{14}B$ material at room temperature, $\mu_0 M_S = 1.63T$, $A = 7.7\times10^{-12} J/m$ and $K_1 = 4.3\times10^6 J/m^3$ [11]. The calculated critical diameter is ~0.2 μm. Sagawa's experimental measurements estimate the critical diameter is ~0.3 μm[12].

The magnetization of a bulk magnet is the sum of the magnetizations attributed to each domain. There are two ways to change the magnetization of a bulk material: (1) domain wall motion and (2) domain rotation. The energy needed for rotating a domain against the anisotropy force is larger than that required to move a domain wall. For a polycrystalline material, if the grain size is larger than the critical diameter, each grain may contain multiple domains, and the change of magnetization is mainly due to the domain walls' motion. If the polycrystalline material is comprised of single-domain crystallites, higher energy is needed to rotate each domain, which would result in a larger coercivity. The coercivity in a polycrystalline magnet can also be reduced if the magnetization of neighboring grain can add to the applied demagnetizing field. This occurs if the individual crystallites are magnetically coupled to each other via a ferromagnetic inter-granular material.

2.5.2 The Phenomenological Model for Understanding the Impact of Microstructure on Hc

The mechanisms that reduce coercivity from anisotropy field H_K can be characterized as falling into two categories: (1) those that are proportional to H_K and (2) those that are proportional to M_S. The general framework[13] describing how the experimentally observed coercivity ($\mu_0 H_C$) is affected by microstructure can be represented by the following formula:

$$\mu_0 H_C = \alpha \mu_0 H_K - N_{eff} \mu_0 M_S \tag{2.11}$$

α characterize the reduction of the ideal anisotropy field. Since the grains in the hot-deformed or sintered magnets are not contact each other directly, which means that there exists grain boundary phase to segregate the neighboring grains, a more detailed analysis[14] distinguishes α into three independent microstructure factors:

$$\alpha = \alpha_K \alpha_\psi \alpha_{ex} \tag{2.12}$$

α_K describes the reduction of the magneto-crystalline anisotropy near the outer shell of grains and it is a function of thickness of this inhomogeneous region r_0 . It is determined by [15-17]:

$$\alpha_K(r_0) = 1 - \frac{{\delta_B}^2}{4\pi^2 {r_0}^2}\left(1 - \sqrt{1 + \frac{4\Delta K {r_0}^2}{A}}\right)^2 \tag{2.13}$$

Where A is the exchange constant, δ_B is the Bloch wall width given by $\delta_B = \pi\sqrt{A/K_1}$ and ΔK denotes the decrease of K_1 in the inhomogeneous region. Bloch wall is the region where the magnetization rotates from the first domain to the second and the rotation is perpendicular to the plane of domain wall. If the magnets have thicker inhomogeneous

region or the materials in this inhomogeneous region have lower anisotropy constant, then α_K will decrease. α_ψ represents the reduction of ideal coercivity due to the effect of misaligned grains. According to the Stoner-Wohlfarth model, which ignores the higher anisotropy terms (K_2, K_3), α_ψ equals to 0.5 when the misalignment ψ is 45° and 1.0 when ψ is 90° or 0°. α_{ex} considers the reduction of ideal coercivity due to the inter-granular exchange interactions, which is typical for nanoscale permanent magnets. If the magnets are comprised of grains perfectly exchange decoupled, then $\alpha_{ex} = 1$. Stronger exchange coupled effect between neighboring grains results in lower α_{ex}. For $Nd_2Fe_{14}B$ magnet, the domain wall width, δ_B, is 4.2nm and the exchange length, $L_{ex} = \sqrt{A/(\mu_0 M_S)}$, is ~2nm. The exchange interaction is a short-range effect and it tries to align the magnetic moment of neighboring grains parallel to each other. Fischer and Kronmüller point out that α_{ex} should be exactly unity for grain diameter is large compared to the range of the exchange interaction[14] and their modeling results show that $\alpha_{ex} = 0.8$ for $\langle D \rangle_{grain} \approx 35nm$ and $\alpha_{ex} = 0.7$ for $\langle D \rangle_{grain} \approx 20nm$. In that ideal case, the short-range exchange effect is negligible. Since there are no magnets are perfectly decoupled, short-range exchange coupling are happened in the hot-deformed and sintered magnets.

N_{eff} takes into account for the internal demagnetization field (stray field) of the sample. The internal demagnetization field depends on the magnetic polarization of the whole sample, thereby it is considered as a long-range interaction. If the grains are coupled with ferromagnetic phase, the altered magnetization of neighboring grains can serve as the

source of an additional field to the demagnetization field, then N_{eff} will increase. The total magnetic energy Φ_G is made up of crystal anisotropy energy Φ_K , exchange energy Φ_A, stray field energy Φ_S, and magnetostatic energy Φ_H in the external field H. It can be expressed as:

$$\Phi_G = \Phi_K + \Phi_A + \Phi_S + \Phi_H \tag{2.14}$$

The stray field energy Φ_S is:

$$\Phi_S = \int -\frac{1}{2}\vec{M}_S \cdot \vec{H}_d d^3 r \tag{2.15}$$

Where H_d represents the demagnetization field due to the magnetic volume charge inside the grains or surface charge on the grain surface. In general, H_d consists of macroscopic stray field H_{macro}, stray field of isolated grain H_g, structural stray field H_{st} and stray field H_S inside the crystallites[17]:

$$H_d = H_{macro} + H_g + H_{st} + H_S \tag{2.16}$$

The macroscopic stray field depends on the macro sample size:

$$H_{macro} = -N_m M_S \tag{2.17}$$

H_g corresponds to the microscopic size of a single crystallite:

$$H_g = -N_g M_S \tag{2.18}$$

H_{st} is due to the hole or non-magnetic participates in the magnet:

$$H_{st} = N_{st} M_S \tag{2.19}$$

H_S depends on the distribution of surface charges of the grains.

2.6 Methods of Manufacturing $RE_2TM_{14}B$ Magnets

2.6.1 Sintering Process

The current commercially manufactured sintered magnets are made by aligning the $Nd_2Fe_{14}B$-based particles (1~10μm) in a magnetic field during compaction into a partially dense solid at room temperature (shown in Figure 2-6). The green compact is then sintered at a higher temperature until it is near full density. A composition that is slightly Nd-rich and Fe-rich with respect to $Nd_2Fe_{14}B$ stoichiometry is used in manufacturing these magnets. A low melting point Nd-rich (Nd-Fe) eutectic phase (grain boundary phase) is found along grain boundaries and at the triple junctions[7]. This phase allows the process to result in a fully-dense bulk magnet. It has been proven that the $Nd_2Fe_{14}B$ grains are magnetically coupled by this grain boundary phase[18]. The SEM image in Figure 2-7 shows the microstructure of the commercially manufactured sintered magnets. The grain size is in the range of 5-10μm, which is large enough to support multiple domains. If the grains in the bulk magnet are large enough to contain multiple domains, an external field which is less than H_K can subsequently demagnetize the grains by moving the domain walls. Typically, Dy is used to substitute for some of the Nd in $Nd_2Fe_{14}B$ to increase the anisotropy field, which leads to an increase in the coercivity of these commercial magnets. Recently a post-sinter Dy diffusion process is used to increase the coercivity with less amount of Dy elements compared to normal sintering process. The post-sinter diffusion process, shown in Figure 2-8, is a vapor deposition of Dy-rich compounds on the surface of $Nd_2Fe_{14}B$-based magnets followed by a heat treatment to diffuse Dy-rich compounds

along the outer shell of the grains. The general idea for the diffusion process is to increase the Dy content in the surface/boundary of the $Nd_2Fe_{14}B$ grain while keeping the grain core at a lower content of Dy. The mechanism by which this is believed to increase coercivity is to "magnetically harden" the periphery of the grain where reverse magnetic domain are believed to nucleate.

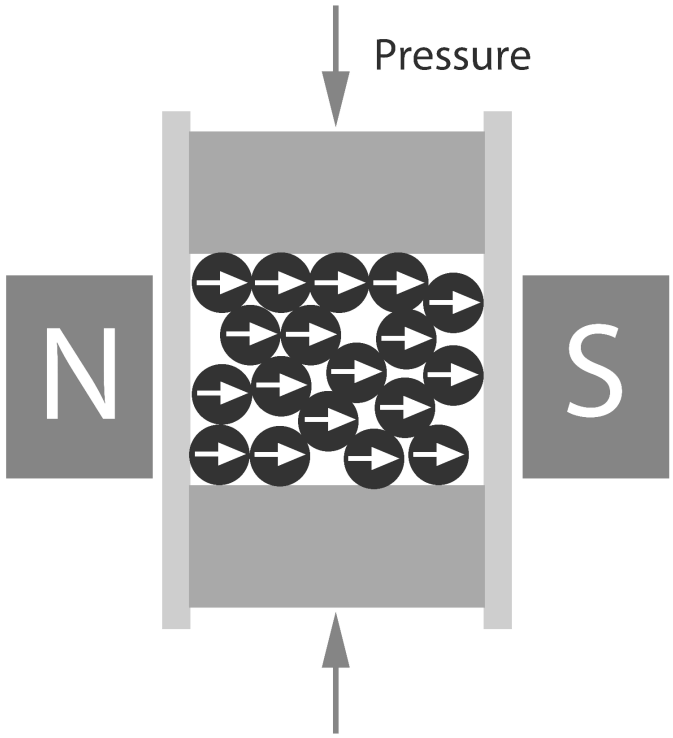

Figure 2-6 Sketch of magnetic press part in the magnetic sintering process

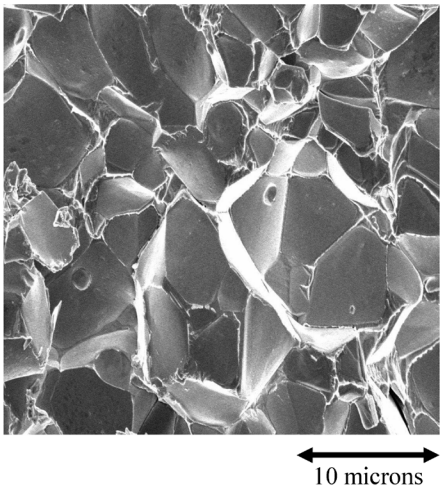

Figure 2-7 Cross-sectional SEM image of sintered magnets.

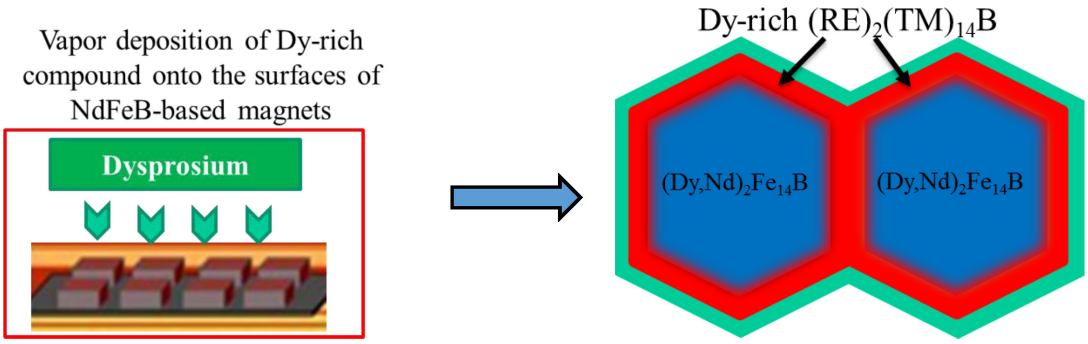

Figure 2-8 Surface Dy diffusion process patterned by Hitachi.

2.6.2 Hot-Deformation Process

The hot deformation approach was first demonstrated by Lee[19] to result in crystallographically-aligned $Nd_2Fe_{14}B$ magnets. A metallurgical approach is used to achieve alignment of grains. No magnetic field is needed. This process results in magnets with submicron grains that are sufficiently small to only support single domains. Hot-deformed magnets have platelet-shaped grains so that [001] direction (easy direction) is perpendicular to the surface of the platelet and parallel to the direction of the applied uniaxial pressure.

Figure 2-9 illustrates the three general steps for manufacturing hot-deformed $Nd_2Fe_{14}B$-based magnetic materials. They are (1) melt-spinning, (2) hot pressing and (3) hot deformation. The high cooling rate of the inductively-melted ingot as it is ejected onto the surface of a spinning Cu wheel results in starting ribbon fragments with submicron randomly oriented grains. The submicron grained ribbons are then consolidated into a solid by applying a pressure of 15-25MPa and heated up to 500°C-600°C in vacuum. The previous two steps result in fully-dense cylinders comprised of randomly oriented submicron grains. The crystallographic alignment of these submicron grains happens during the hot deformation step. A uniaxial pressure ranging from 20MPa to 50MPa is applied to deform the cylinder, which is held at a higher temperature (600°C-800°C) in a larger die to reduce the height of the cylinder by 60% to 80%, while increasing the cross-sectional area. Figure 2-10 compares the microstructure of bulk magnets made by sintering and hot-deformation process. The microstructure of hot-deformed magnets is dramatically different from that of the sintered magnets. It is obvious that hot-deformed magnets consist

of grains which are an order of magnitude smaller than that in sintered magnets. The mechanism by which crystallographic alignment occurs depends critically on the presence of the Nd-Fe intergranular eutectic phase. This mechanism is described in the following section.

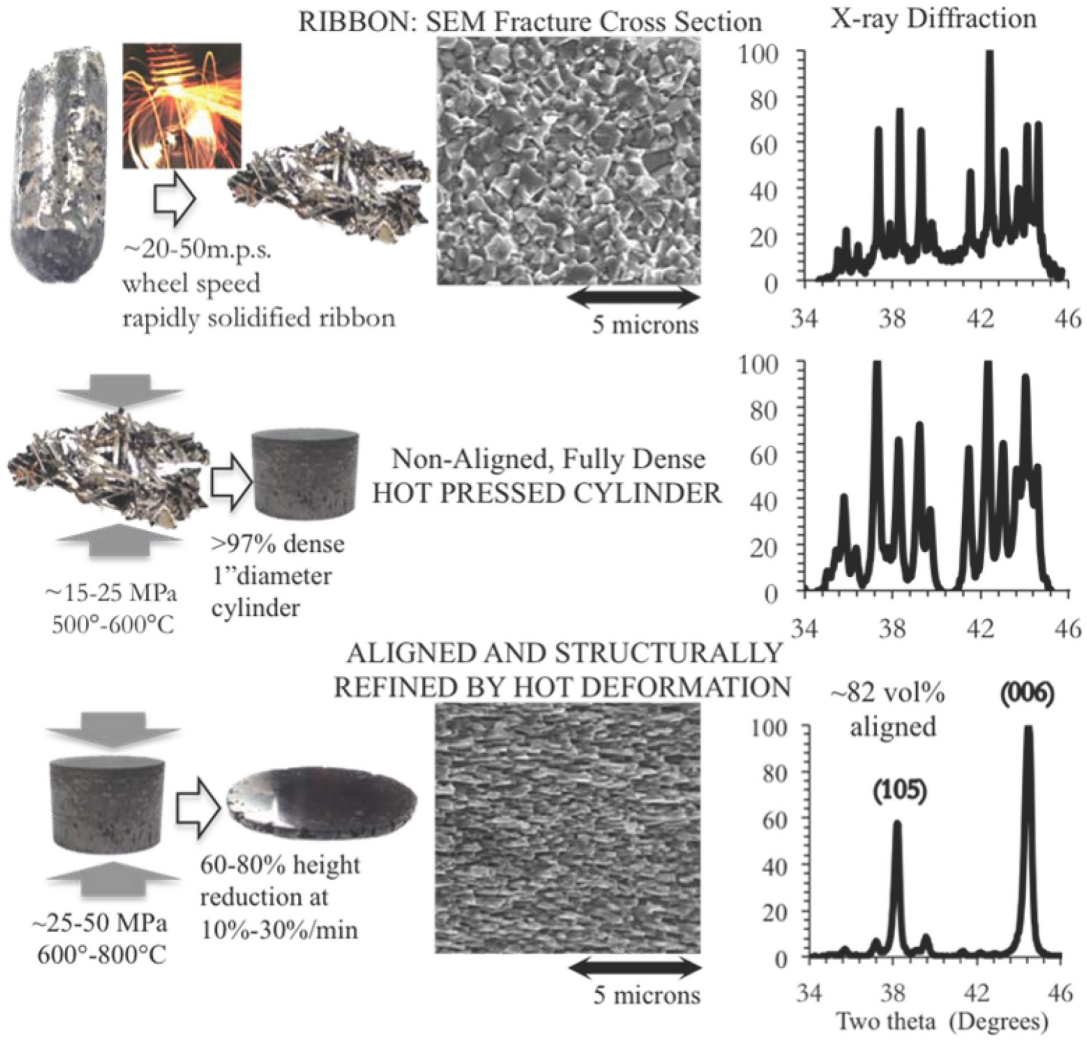

Figure 2-9 General steps of hot-deformation process: (1) melt-spining, (2) hot pressing and (3) hot deformation

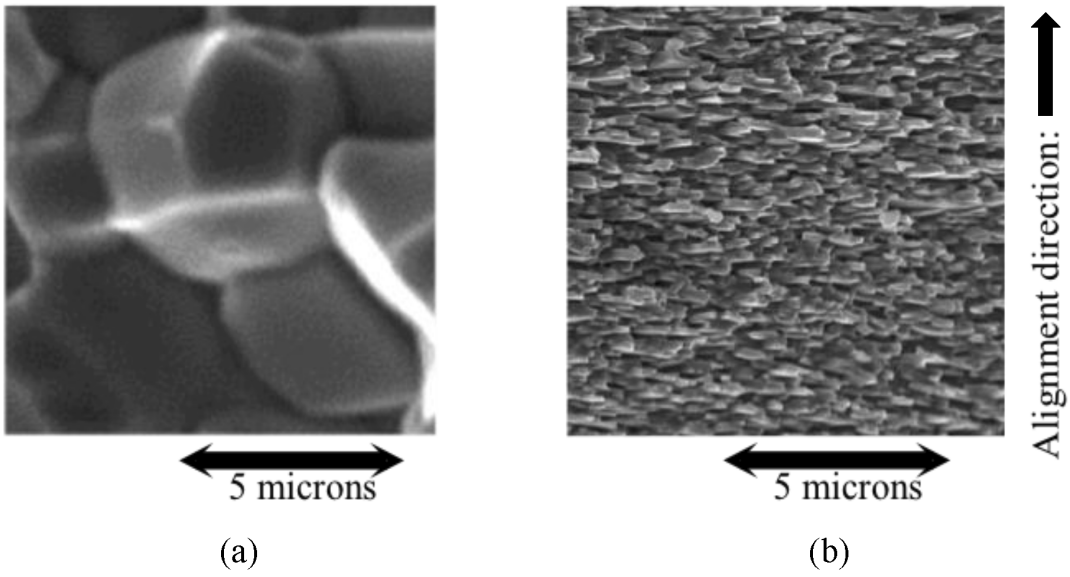

Figure 2-10 Microstructures of (a) sintered magnets and (b) hot-deformed magnets measured by SEM.

2.6.3 Preferential Dissolution/Re-precipitation Mechanism

The particular microstructures of hot-deformed magnets, the degree of alignment, the driving force and the phenomena's kinetics can be explained by the preferential dissolution/re-precipitation mechanism proposed by Li and Graham[20]. $Nd_2Fe_{14}B$ grains whose [001] directions are not aligned along the direction of the applied uniaxial pressure will dissolve into the Nd-rich eutectic liquid at the hot deformation temperature, then diffuse and precipitate onto the sides of the aligned $Nd_2Fe_{14}B$ grains whose [001] directions are aligned along the direction of the applied pressure. The driving force is the difference of elastic energy ($\Delta\mu$) between aligned and non-aligned $Nd_2Fe_{14}B$ grains due to the crystallographic anisotropy in the elastic modulus of $Nd_2Fe_{14}B$ at elevated temperatures. Non-aligned grains have higher total elastic energy than aligned grains. The large energy

difference between these two types of grains causes more non-aligned grains to diffuse into the Nd-rich eutectic phase, which will improve the crystallography texture of the magnets. As a result, non-aligned isotropic grains will dissolve into the liquid phase and then precipitate on the surface of aligned isotropic grains to form the platelet structure. This results in a characteristic aspect ratio of the platelet-shaped grains is ~3:1. As diagramed in Figure 2-11, only about 1 out of every 27 isotropic crystals in a randomly oriented material has its [001] direction along the direction of the applied uniaxial pressure and thus does not dissolve.

The energy difference are proportional to the square of stress (σ^2):

$$\Delta\mu \propto \sigma^2 \tag{2.20}$$

When the strain rate is constant, the stress is exponentially proportional to the temperature. Their relationship is expressed as:

$$\sigma \propto \exp(\frac{\Delta G_{vis}}{2RT}) \tag{2.21}$$

where ΔG_{vis} (>0) is the activation energy of viscosity.

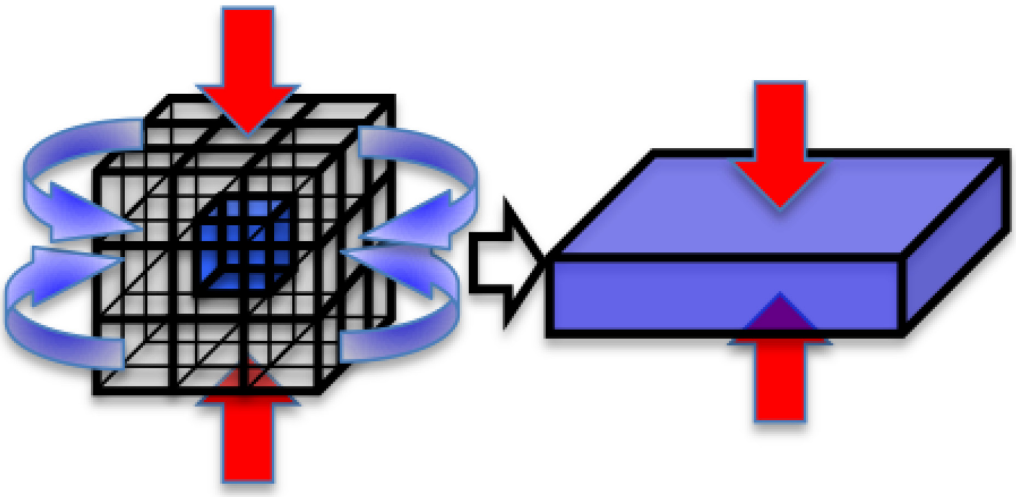

Figure 2-11 Under uniaxial pressure at elevated temperatures, the non-oriented $Nd_2Fe_{14}B$ crystals in the randomly oriented solid have higher strain energy and so preferentially dissolve in the liquid Nd-rich eutectic and re-precipitate on the sides of the nearest un-dissolved [001] oriented grain resulting in a magnet comprised of self-aligned [001] platelet submicron magnets

This model concludes that in order to increase the texture of the magnets, high stress and low temperature should be considered. Kwon and Yu[21] also find that if the temperature is too high, the elastic energies of both grains will be reduced and the energy difference may also be decreased. Under these circumstances, fewer unfavorable grains can be dissolved into the eutectic phase and it will result in a low alignment of the grains and therefore inferior magnetic properties. However, $Nd_2Fe_{14}B$-based magnets are brittle due to their crystallographic structure. Excessively high stress at low temperature can cause cracks in the magnets. Thus, the stress, strain rate, temperature and loading time should be balanced to optimize the alignment of grains and hot workability.

Temperature not only has obvious effect on the deformation process and the hot workability, but also on the grain size of the magnets. The grain size has an impact on the diffusion path of the grains. A larger grain size will make non-aligned grains less likely to dissolve into the eutectic phase. Therefore, initially melt spun ribbons with small grain sizes are a prerequisite. Additionally, the temperature of hot deformation and loading time should be constrained to slow down the growth speed of the grains. Proper temperature and higher pressure are very important to control the microstructure of the hot-deformed magnets.

In summary, there are five process variables that may influence the degree of alignment of the transformed material: (1) deformation temperature, (2) applied uniaxial pressure, (3) volume fraction of eutectic phase, (4) melting point of the eutectic phase, (5) grain size of un-deformed magnets.

2.7 The Effect of Intergranular Phase on Magnetic Properties

Table 2-1 Other research work on analyzing the impact of intergranular phase on magnetic properties of $Nd_2Fe_{14}B$-based materials

Materials	Eutectic phase	$Nd_2Fe_{14}B$ size	α	N_{eff}
Thin film[22]	Nd-Fe	~50-100nm	0.26	0.42
Thin film[22]	Nd-Ag	~50-100nm	0.41	0.05

The work done in this section will show the existing experimental evidence that non-Fe-containing eutectic phase can improve coercivity. Cui[22] et al investigated the effect of

the non-ferromagnetic inter-granular phase on increasing the coercivity. They deposited an Nd-Ag/Nd-Cu layer into the $Nd_2Fe_{14}B$-based thin film comprised of single-domain grains. Due to its lower melting point than $Nd_2Fe_{14}B$, Nd-Ag/Nd-Cu infiltrates the grain boundary phase at the temperature above the eutectic melting point. Data in Table 2-1 clearly illustrates that the N_{eff} of a thin film with the non-ferromagnetic intergranular phase Nd-Ag decreases dramatically from the value seen in the film with ferromagnetic intergranular phase. This indicates that the self-demagnetization field in $Nd_2Fe_{14}B$ grains is reduced by the decrease of surface defects where the nucleation of reverse domains are believed to occur. The increase of α may be due to the decrease of exchange coupling between the neighboring grains. Their work is found as evidence that magnetic isolation of single-domain grains caused by non-magnetic grain boundary phase can effectively increase α and decrease N_{eff}.

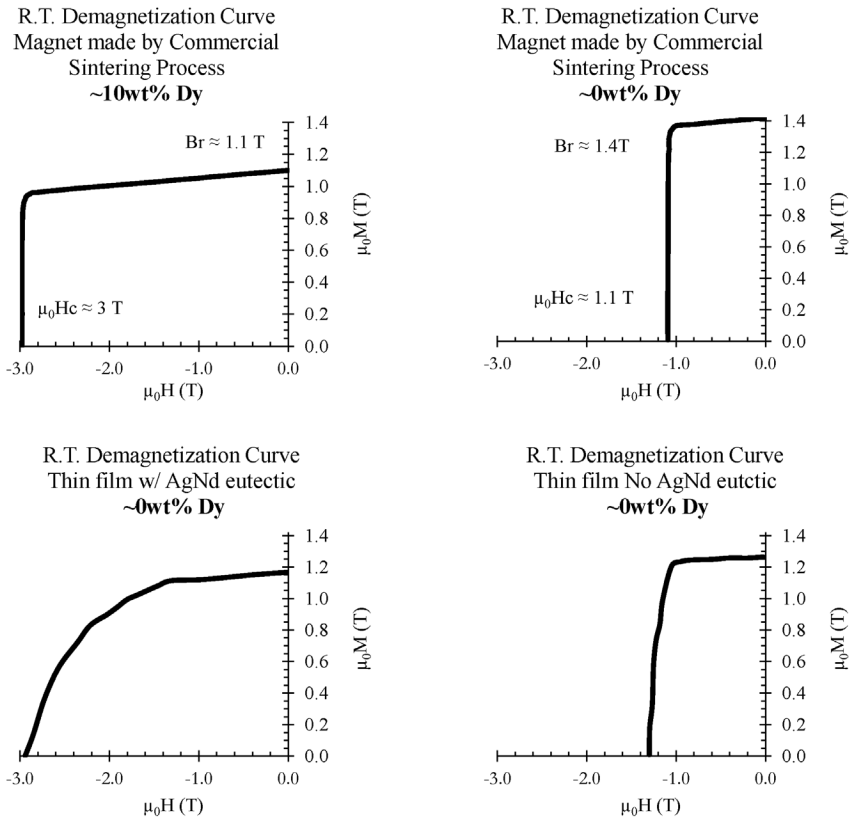

Figure 2-12 Cui's thin film Dy-free material exhibits an H_C comparable to that of the conventionally manufactured bulk material with 10%wt Dy only when the constituent submicron magnets are magnetically isolated by a thin layer of the inter-granular non-Fe-containing eutectic.

The room temperature demagnetization curves from Cui's thin films with and without the Nd-Ag eutectic phase are compared to those from commercially manufactured sintered magnets containing 10wt% Dy and 0wt% Dy in Figure 2-12. The coercivity and remanence of Dy-free thin film with magnetically isolated grains are comparable to those of the commercially manufactured sintered magnet with 10wt% Dy, which is currently used in traction motors. Cui's result shows that the non-ferromagnetic inter-granular phase can dramatically increase the coercivity. If magnetic isolation of single-domain crystallites

could be achieved in bulk material, a large increase in coercivity would be expected as seen in the thin film. There are some other research work [23-27] indicate that preventing magnetic coupling through the use of a non-magnetic inter-granular phase may be effective in increasing the coercivity of bulk magnets and powders [28]. In these cases, the degree to which the coercivity was enhanced was likely limited by the non-uniformity of the intervening inter-granular phase, or the large size of the constituent $Nd_2Fe_{14}B$ crystallites. At the time this research was performed, none of the methods resulted in a bulk magnet consisting of single-domain crystallites that are magnetically isolated from each other.

Recent work done by Akiya[29, 30] and Sepehri-Amin[31] showed that coercivity can be improved by infiltrating Nd-Cu alloy into the grain boundary regions for the hot-deformed $Nd_2Fe_{14}B$-based material. As the grain size for hot-deformed magnets are nanoscale, and the area of grain boundary per unit volume is very high, it needs a large amount of Nd-rich alloy to cover the magnet and be diffused into the grain boundary regions. Instead of using the grain boundary diffusion process, a more effective manufacturing process based on hot-deformation process is used in this work to improve the coercivity with reduced Dy content.

To obtain bulk materials with the lowest impact of microstructure on the reduction in H_C from H_K, there are three characteristics that are important: (1) small enough grains must be generated in the bulk materials so that each grain is capable of supporting only a single magnetic domain; (2) the individual grains must be crystallographically-aligned; and (3) the neighboring grains cannot be magnetically coupled by a Fe-rich inter-granular eutectic phase.

Chapter 3

Experimental Techniques

The microstructural properties of magnets play an important role in remanence and coercivity of materials. In this chapter, the experimental techniques used to characterize the grain size and crystallographic alignment will be described. The instrument used to measure the magnetic properties of materials at different temperatures will be introduced.

3.1 Grain Size Measurement

The intercept technique (Figure 3-1) is used to estimate the grain size from SEM micrographs. In this method, one or more random lines are drawn on the SEM micrographs. Then, the average grain size can be determined by dividing the number of grains that intersect those lines by the true line length. Grains that intersects with the end of the line count as half grains.

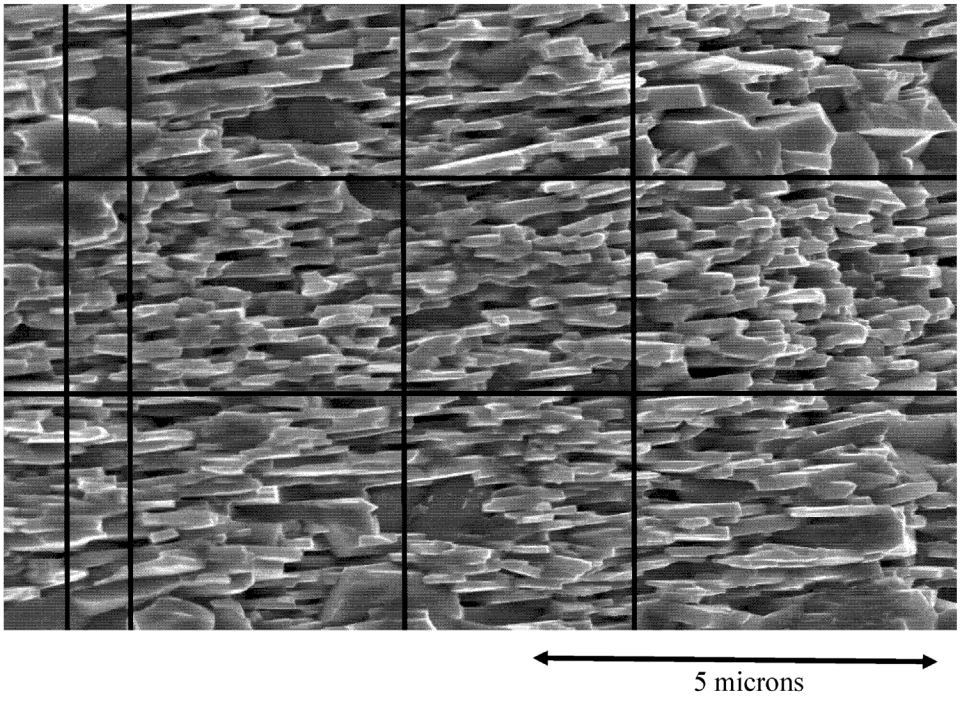

Figure 3-1 The intercept technique used to measure the grain size of the magnets

3.2 Developing a Quantitative Metric of Crystallographic Alignment

In this section, a method is described to quantify the crystallographic alignment for $RE_2TM_{14}B$-based permanent magnets by analyzing the Bragg-Brentano X-ray diffraction data. Crystallographic alignment is essential to the resulting remanence (B_r) of a permanent magnet. The X-ray pole figure approach[32] is a conventional way to fully reveal the crystallographic alignment information of the polycrystalline materials. However, the time required for data collection for this method is prohibitive. Crystallographic alignment of

magnets has also been characterized by many research groups by using the diffracted intensity of (006) peak and the peak width at half maximum intensity [33-37]. However, with this method there exists large variations of peak intensities when the sample is rotated about the alignment axis. Some groups only analyze the effect of aligning field on the remanence of the sample. All results show that higher crystallographic alignment results in higher remanence, but the exact percentage of alignment and the mathematical relationship between the crystallographic alignment and remanence are not clear. The method used in this work quantitatively estimates the crystallographic alignment by analyzing XRD data.

X-ray diffraction (XRD) techniques are used to characterize the crystallographic alignment information of the polycrystalline magnetic materials. The relative intensities of diffraction peaks in the 2θ range for each sample are measured by a symmetric Bragg-Brentano diffraction geometry using Cu K_α radiation. The 2θ step size of 0.025° and counting time of 8sec/step are used to precisely measure the intensities of each peak. The lattice constants are initially determined by analyzing the peak positions of two major peaks. Then, the peak position of each individual peak is calculated according to the lattice constants and Bragg's law. The peak fitting analysis is completed by using Lorentz peak shapes, and the resulting R-squared value is larger than 0.98.

For $Nd_2Fe_{14}B$-based material, the uniaxial magnetocrystalline easy direction of magnetization is in the [001] crystallographic direction (c-axis), and the directions perpendicular to [001] are the magnetocrystalline hard directions. The Powder Diffraction File (PDF) for $Nd_2Fe_{14}B$ (card #88-2285) shows that there are 23 (hkl) peaks in the 34°~46°

2θ range, which cover the majority of the reflection peaks. Thus, this 34°~46° 2θ range is selected as the XRD scan range. In an unaligned polycrystalline $Nd_2Fe_{14}B$ material, illustrated in Figure 3-2, the easy direction of each single crystallite deviates from the surface normal of the sample by an unknown amount. In an aligned polycrystalline $Nd_2Fe_{14}B$ magnets, there are usually two major peaks (105) and (006) shown in the XRD data. The normal of (006) planes are parallel to the easy direction and the normal of (105) planes are tilted ~16° from the easy direction. Those two planes are considered well aligned planes and the intensities of the two corresponding (hkl) reflection peaks are used to estimate the degree of crystallographic alignment of polycrystalline samples in the subsequent analysis.

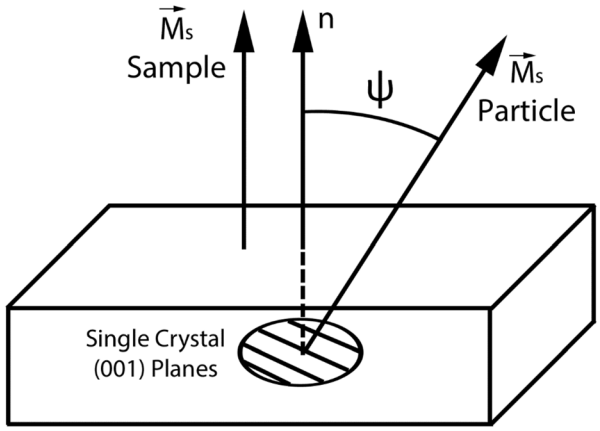

Figure 3-2 A polycrystalline sample with a single crystallite shown whose easy axis is Ψ degree off the surface normal of the sample.

In a symmetric Bragg-Brentano diffraction measurement from a polycrystalline sample, the intensity observed for a particular (hkl) diffraction peak is proportional to the product:

$$I_{obs} \propto \left|F_{hkl}\right|^2 \left|LP\right|\left|F_T\right|\left|vol\%_{hkl}\right| \tag{3.1}$$

where F_{hkl} is the structure factor, LP is the Lorentz-polarization factor, F_T is the temperature factor, and $vol\%_{hkl}$ is the volume percentage of the sample with the (hkl) plane situated with respect to the surface normal.

In a randomly oriented polycrystalline sample, the (hkl) families of planes resulting in a diffraction peak are proportional to the multiplicity factor m_{hkl}. The intensities for (hkl) peaks would be observed in a diffractor from a randomly oriented sample and are proportional to:

$$I_{ICDD} \propto \left|F_{hkl}\right|^2 \left|LP\right|\left|F_T\right|\left|m_{hkl}\right| \tag{3.2}$$

The vol% of the randomly oriented material with their magnetically easy directions [001] within ψ degrees of the surface normal should therefore be estimated by the ratio of multiplicities:

$$Vol\% = \frac{V_{oriented}}{V_{all}} = \frac{\sum_{\substack{all \text{ (hkl) peaks with angle } \psi \\ \text{or less apart from (001)}}} m_{hkl}}{\sum_{\text{all (hkl) peaks in } 2\theta \text{ range}} m_{hkl}} \tag{3.3}$$

For a randomly oriented polycrystalline $Nd_2Fe_{14}B$ material, the vol% of oriented crystalline grains calculated based on Equation (3.3) is:

$$Vol\% = \frac{V_{oriented}}{V_{all}} = \frac{m_{(105)} + m_{(006)}}{\sum_{\text{all (hkl) peaks in } 34°\sim46° \text{ range}} m_{hkl}} = 4.1 vol\% \tag{3.4}$$

In a randomly oriented polycrystalline sample, the vol% of crystallite with any particular direction ψ is proportional to the surface area dA, illustrated in Figure 3-3. For $Nd_2Fe_{14}B$ materials, the crystallites whose normal is within ~16° to the [001] direction are taken into account. The vol% of oriented crystallites in the magnet can be calculated as:

$$Vol\% = \frac{V_{oriented}}{V_{all}} = \int_0^{\varphi=16^\circ} \frac{r \cdot 2\pi r \cdot \sin\varphi}{2\pi r^2} d\varphi = \int_0^{\varphi=16^\circ} \sin\varphi d\varphi = 1 - \cos(16^\circ) = 3.9\% \quad (3.5)$$

Equation (3.5) yields that only ~3.9vol% of the sample would be so oriented. This result indicates that the ratio between the sum of multiplicities for (hkl) peaks within ~16° of the (001) peak and the sum of all (hkl) peaks is a robust estimation for the degree of crystallographic alignment.

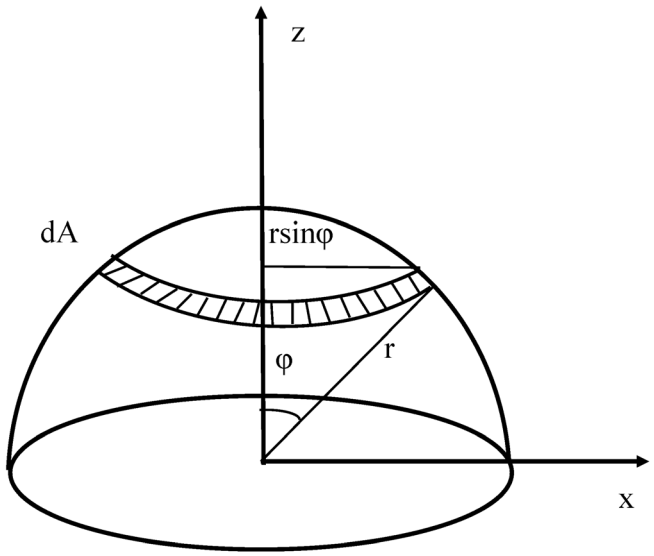

Figure 3-3 Volume percent of crystallite with any particular direction ψ is proportional to the area dA.

A magnet with sufficient remanence and coercivity ($\mu_0 H_C$) is desired to have an order of magnitude higher vol% oriented than that of randomly oriented magnet. If a polycrystalline $Nd_2Fe_{14}B$ magnet has a preferred orientation, then the degree of alignment can be assessed from the intensities of the observed diffraction peaks:

$$Vol\% = \frac{Vol\%_{(105)} + Vol\%_{(006)}}{\sum_{\substack{\text{all (hkl) peaks in} \\ \text{the 34°~46° range}}} Vol\%_{(hkl)}} = \frac{\dfrac{I_{obs}}{\left|F_{hkl}\right|^2 \left|LP\right|\left|F_T\right|_{(105)}} + \dfrac{I_{obs}}{\left|F_{hkl}\right|^2 \left|LP\right|\left|F_T\right|_{(006)}}}{\sum_{\substack{\text{all (hkl) peaks in} \\ \text{the 34°~46° range}}} \dfrac{I_{obs}}{\left|F_{hkl}\right|^2 \left|LP\right|\left|F_T\right|_{(hkl)}}} \tag{3.6}$$

Since the value of relative intensities (I_{PDF}) in the powder diffraction file are proportional to $\left|F_{hkl}\right|^2 \left|LP\right| F_T \left|m_{hkl}\right|$, the degree of crystallographic alignment can be written in terms of I_{obs} , I_{PDF} and m_{hkl} :

$$Vol\% = \frac{\dfrac{I_{obs}}{I_{PDF}/m_{(105)}} + \dfrac{I_{obs}}{I_{PDF}/m_{(006)}}}{\sum_{\substack{\text{all (hkl) peaks in} \\ \text{the 34°~46° range}}} \dfrac{I_{obs}}{I_{PDF}/m_{(hkl)}}} \tag{3.7}$$

3.3 Measuring Remanence and Coercivity with VSM

A vibrating sample magnetometer (VSM), invented by Simon Foner at Lincoln Laboratory MIT, operates based on Faraday's Law of Induction to measures magnetic properties of samples. As shown in Figure 3-4, a small cubic sample (< $3mm^3$) is attached to one end of the vibrating nonmagnetic rod. The electromagnet gives a large enough magnetic field to magnetize the sample. The magnetic dipole moment of the sample will produce a magnetic field near it. When the sample is vibrating, the change of magnetic flux will induce an alternating electromotive force (emf) in the pick-up coils. The induced electromotive force

is proportional to the magnetization of the sample. Larger magnetization of the sample results in larger electromotive force. The VSM measurement is very sensitive and it can measure the magnetic properties of both strong and weak magnets. Since only the sample and rod will be heated or cooled, a VSM instrument can measure the magnetic properties of samples at different temperatures.

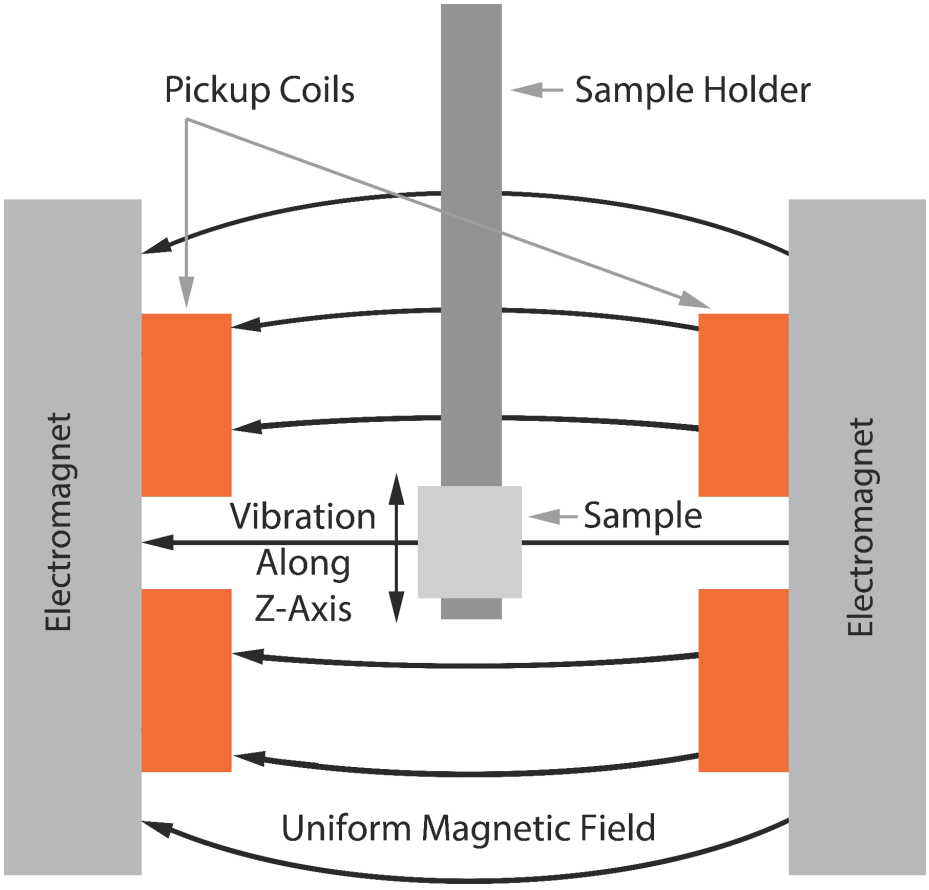

Figure 3-4 Sketch of VSM instrument

Chapter 4

Characteristics of $RE_2TM_{14}B$ Magnets Used in Traction Motors of Hybrid and Electric Vehicles

The work described in this chapter is designed to address task #1, to determine the minimum amount of Dy needed in bulk $RE_2TM_{14}B$ magnets based on currently commercially manufacturing processes. It examines the temperature-dependent demagnetization of sintered $RE_2TM_{14}B$ magnets with different stoichiometries. A subset of the commercially manufactured magnets has been subjected to diffusion processes that have been claimed to lead to a higher resistance to demagnetization than would otherwise be the case. This report first examines the extent to which the wt% (weight percent) of Dy in the magnet determines the high temperature coercivity ($\mu_0 H_C$) given the range of other

differences in stoichiometry and degree of crystallographic alignment between the magnets examined. Second, the data is analyzed to determine whether the diffusion process has a measurable impact on the $\mu_0 H_C$ of the magnets. Third, the minimum amount of Dy needed in non-diffused and diffused magnets which could potentially be used in traction motors of electric and hybrid vehicles is estimated.

4.1 Structure of the Experiments

Seven commercially manufactured sintered magnets (three non-diffusion processed and four diffusion processed) from three vendors are examined in this work. The chemical compositions of these magnets measured by ICP (Inductively Coupled Plasma) are represented in Table 4-1. The degree of crystallographic alignment is estimated by analyzing X-ray diffraction data, which was described in the previous chapter. The demagnetization curves of these magnets at three different temperatures (25˚C, 100°C, 160°C) is measured by using a Vibrating Sample Magnetometer (VSM). The magnetic data is then analyzed in light of the differences in stoichiometry and crystallographic alignment to prove whether or not Dy content and having undergone a diffusion process are the primary indicators of the high temperature coercivity.

Table 4-1The chemical compositions of the materials examined in this work

Diffusion Treatment?	Vendor	Sample Name	wt% Dy	wt% Pr	wt% Nd	wt% Tb	wt% Co	wt% Fe	wt% B	wt% R.E.	wt%TM	wt%B	wt% FLUXING Agents (Ga,Al,Cu,Zr)	Estimated at% RE-rich inter-granular phase at 750C
NO	MTU	Hot Deformed Magnet	2.6	7	20.9	0	4.0	64.1	0.9	30.5	68.1	0.9	0.5	4.0
NO	TRIDUS	N505H-S unplate before treatment 10-24-12	0.1	6.7	22.1	0.0	0.8	69.2	1.0	28.9	70.0	1.0	0.1	2.5
YES	TRIDUS	PR4952GY002	0.6	6.3	21.9	0.0	0.8	69.3	1.0	28.8	70.1	1.0	0.1	2.4
YES	ZH MAG	48NB40-30-2.5 AT (M L 2)	1.5	4.7	26.6	0.0	0.4	65.6	1.0	32.8	66.0	1.0	0.2	6.6
NO	ZH MAG	42SB40-30.2.7 (before-treatment)	3.9	6.1	19.1	0.0	1.4	68.3	1.0	29.1	69.7	1.0	0.2	2.6
YES	ZH MAG	42SB44.3-18-2.6 AT (M L 1)	4.1	5.8	22.0	0.0	1.6	65.3	1.0	31.9	66.9	1.0	0.2	5.5
NO	ZH MAG	40UB12.5-12.5-5 (before-treatment)	5.3	5.5	17.5	0.6	2.3	67.6	1.0	28.9	69.9	1.0	0.2	2.3
YES	ZH MAG	40UB12.5-12.5-5 (after-treatment)	6.0	6.1	19.2	0.7	2.5	64.2	1.1	32.0	66.7	1.1	0.2	5.9

4.2 Results and Discussion

As can be seen in Table 4-1, the Dy content of commercially manufactured magnets varies from 0.1wt% to 6.0wt%. The other noticeable variations include Pr and Co content varying from 4.7wt% to 6.7wt% and 0.4wt% to 2.5wt%, respectively. The variations in the wt% of Co and Pr and in crystallographic alignment do not coincide with the variations in wt% of Dy. The X-ray diffraction data of each sintered magnet are shown in Figure 4-1, in which the intensity of the sixth order diffraction peak from the (001) planes, labeled (006), and the first order diffraction peak from the (105) planes, labeled (105), both increase with volume percent (vol%) of aligned grains in the bulk magnet. The results show that vol% of crystallographic alignment of samples varies from 55vol% to 78vol%. According to a geometric result estimated in Chapter 3, if the grains in the material are randomly orientated, only 3.9vol% of the material has their c-axes within ~16° of the press direction.

The demagnetization curves recorded from the seven sintered magnets at different temperatures are illustrated in Figure 4-2. Figure 4-3 gathers the magnetic data of those sintered magnets as a function of wt% of Dy content. The circular data points are the $\mu_0 H_C$ of commercially manufactured magnets made without an added Dy diffusion process and the square data points correspond to the commercially manufactured magnets produced with a post-sinter Dy diffusion process.

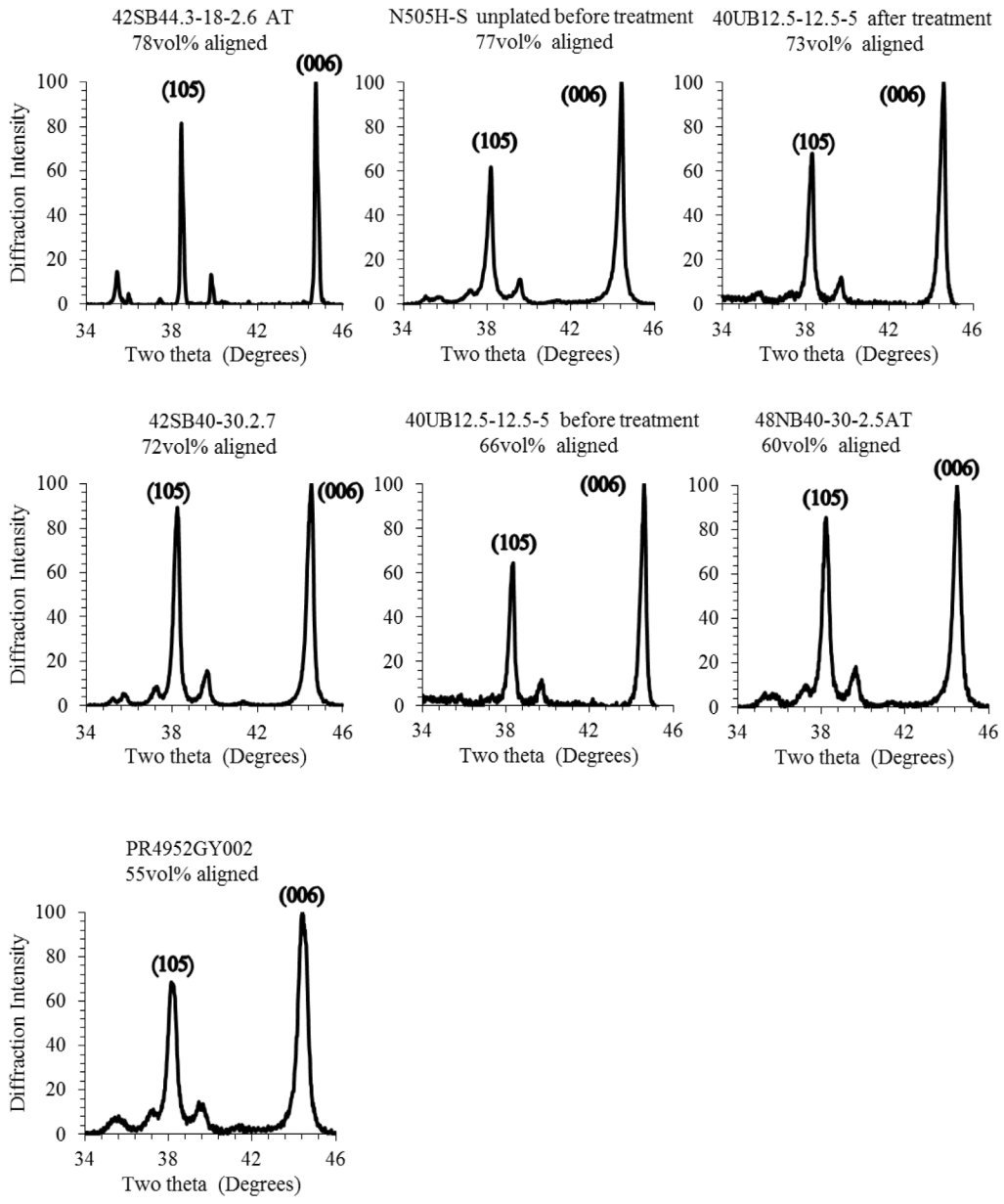

Figure 4-1 X-ray diffraction data of seven commercially manufactured magnets.

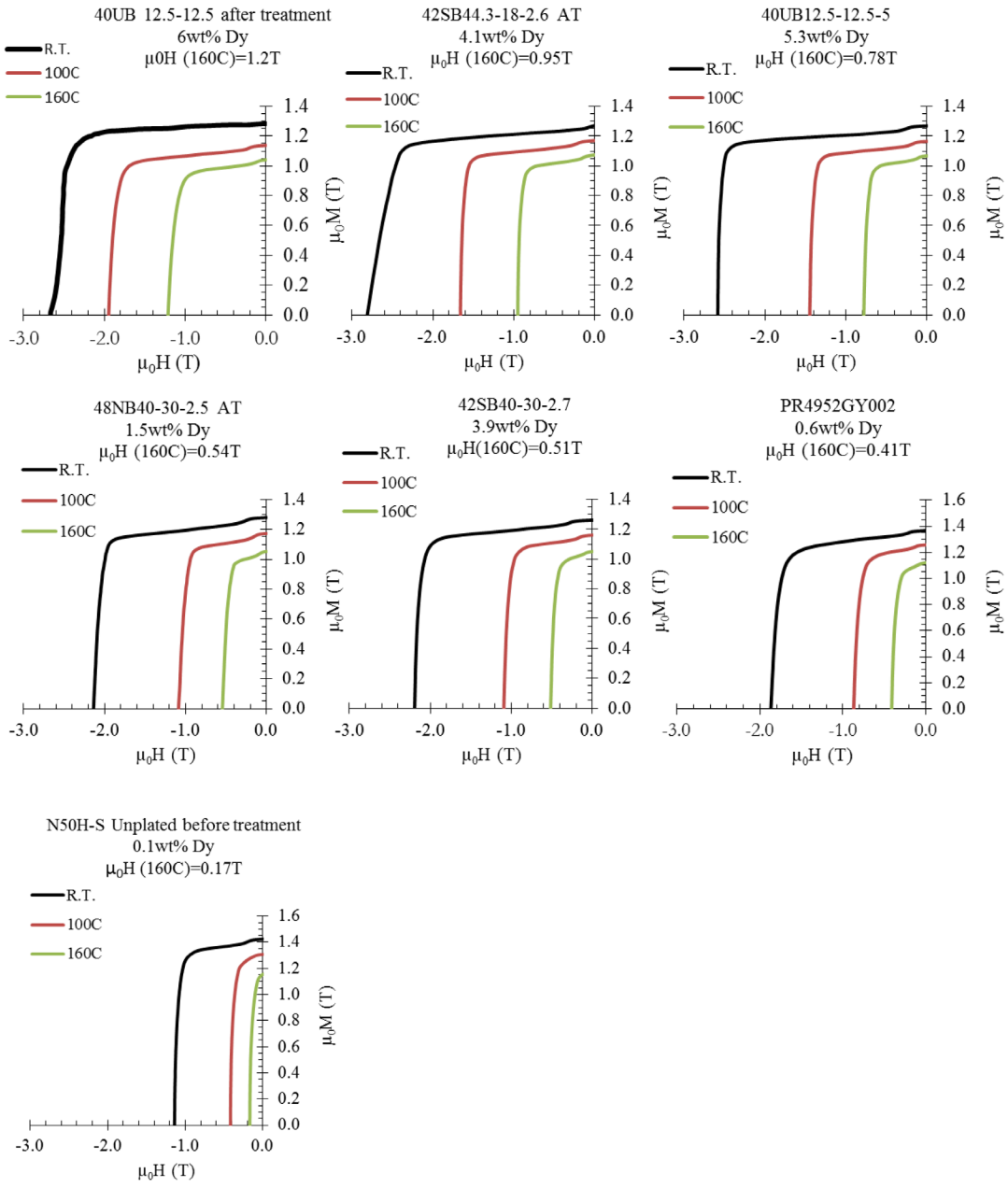

Figure 4-2 Demagnetization curves of seven commercially manufactured magnets.

Despite the differences in other elements used in the magnets (Table 4-1), and the differences in crystallographic alignment, the coercivity has a linear relation with the wt% of Dy content. The lines drawn through the data points are a linear regression of the data based on least square fitting method. Apparently, the impact on coercivity of increasing "x" in $(1-x)Nd_2Fe_{14}B - xDy_2Fe_{14}B$ due to the higher anisotropy coefficients of $Dy_2Fe_{14}B$ is much more pronounced than the impact of other stoichiometric variations. This relationship is evident at all temperatures. Dy-diffusion treatments can clearly be seen to have an impact on coercivity in addition to the impact of just adding more Dy as can be noticed by the different linear relationship observed for Dy-diffused samples and non-diffused samples. For non-diffused samples:

$$\mu_0 H_{C,160^\circ C}(\pm \sim 0.08T) = 0.14T + 11.2 \times wt\%Dy \tag{4.1}$$

And for diffused samples:

$$\mu_0 H_{C,160^\circ C}(\pm \sim 0.01T) = 0.32T + 14.9 \times wt\%Dy \tag{4.2}$$

Nevertheless, the remanence decreases as the wt% of Dy increases. The reason for that is the magnetic moment orientation of Dy-Fe coupling is in the opposite direction of Fe-Fe coupling and Fe-Nd coupling. Both coercivity and remanence decrease as temperature increase because of thermal fluctuations.

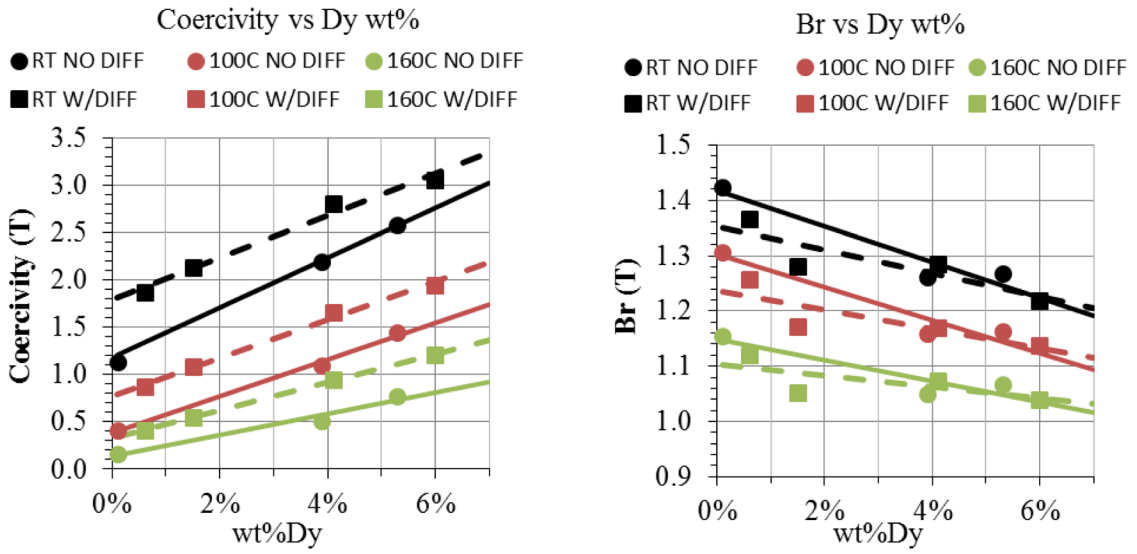

Figure 4-3 Coercivity and remanence of commercially manufactured magnets with and without a subsequent Dy diffusion process at varying temperature.

Diffusion treatment of the sintered magnets clearly reduces the amount of Dy needed for magnets used in the traction motors of electric and hybrid vehicles. The application requires magnets to have $\mu_0 H_C =\sim 0.9T$ and $B_r =\sim 1.0T$ at 160°C. In order to visualize the extent of Dy reduction in the commercially manufactured magnets made by different process, a horizontal line of $\mu_0 H_C = 0.9T$ is superimposed on the 160°C coercivity data, shown in Figure 4-4. The intersection is the amount of Dy needed in the magnets corresponding to different processes. It can be concluded that the minimum amount of Dy needed for sintered magnets to be used in the traction motors of electric and hybrid electric vehicles is reduced from ~7wt%Dy to ~4wt% Dy if a post-sinter diffusion process is applied. The B_r for non-diffused magnets containing ~7wt% Dy and diffused magnet

containing ~4wt% Dy are 1.02T and 1.06T at 160°C. The remanences for both magnets satisfied the requirement for the electric and hybrid vehicles application.

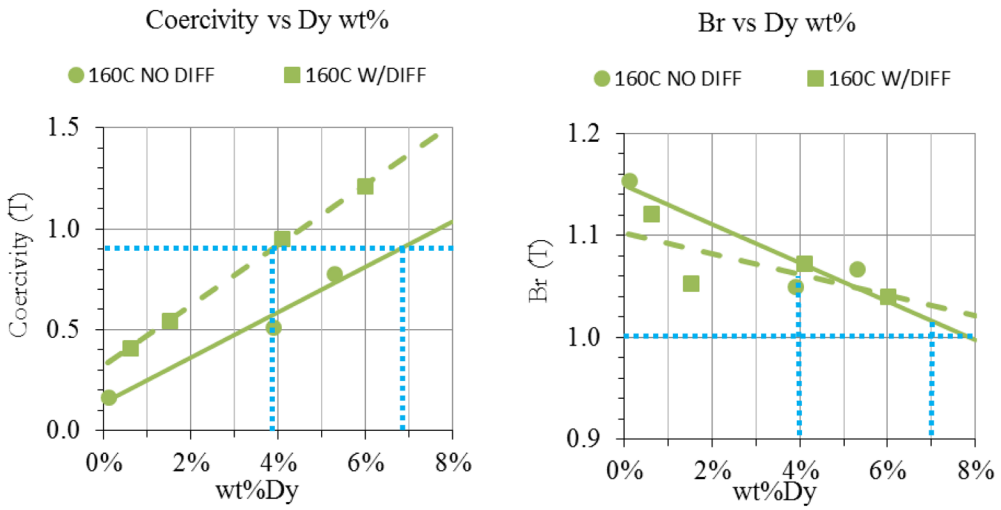

Figure 4-4 Coercivity of commercially sintered magnets at 160°C.

4.3 Conclusions

The conclusions drawn from this report are summarized as follows. First, the wt% of Dy is the primary indicator of high temperature coercivity. The morphological variations in degree of magnetic alignment and that the variations in the amount of Co, Pr, and Tb, eutectic phase, and fluxing agents over the ranges examined have a small to negligible impact on the high temperature resistance to demagnetization of these magnets. Second, quantitative expressions to predict the high temperature coercivity and remanence of these magnets have been formulated for both diffusion treated and non-diffusion treated

magnets. Third, the diffusion process clearly reduces the amount of Dy needed for increasing high temperature coercivity.

Chapter 5

Impact of Hot-deformation Parameters on Microstructural and Magnetic Properties of $RE_2TM_{14}B$ Magnets

The goal of the research shown in this chapter is to manufacture bulk $RE_2TM_{14}B$ magnets consisting of crystallites which are small enough to support single domains. In this chapter, the impact of hot-deformation parameters on grain size, coercivity and remanence of each sample (Task #2) is discussed. Hot-deformation is a thermomechanical process used to produce fully dense crystallographically aligned magnets from melt-spun ribbons. Temperature and stress are the key parameters for the hot-deformation process. Optimization of the hot deformation process parameters can improve the microstructure of the magnets and thereby enhance the magnetic properties. The work shown in this chapter

first examines the microstructural properties of magnets that were hot-deformed at different deformation temperatures. The hot-deformation mechanism is studied based on the model of preferential dissolution/re-precipitation mechanism. This work also analyzes the effect of hot-deformation parameters on the magnetic properties of the magnets. Finally, the optimal hot-deformation parameters that apply to the manufacture of $RE_2TM_{14}B$ magnets consisting of submicron crystallites are determined.

5.1 Experimental Design

The initial melt-spun ribbon particles used for the hot-deformation process were made by the Magnequench Company. The chemical composition of the ribbon is 2.6wt% Dy, 7.0wt%Pr, 20.9wt% Nd, 0.9wt%B, 4.0wt% Co, 0.5wt%Ga, and 64.1wt% Fe. The ribbon particles are first consolidated under vacuum to >95% theoretical density at ~610°C by applying approximately 45MPa of pressure for 10 minutes. Then, the ~1cm tall × 1.9cm diameter fully dense cylinders are designed to be reduced by ~70% of their initial height over a few minutes, again in vacuum, by applying a uniaxial pressure ranging from ~20 to ~63MPa at temperatures between ~680°C to ~900°C. The strain rate for all the samples are controlled between $0.014s^{-1}$ and $0.020s^{-1}$. The resulting hot-deformed magnets are discs approximately 3mm in height and 4cm in diameter. Cubes with dimension of ~ $3mm^3$ were cut from the center of bulk magnets using electric discharge machining (EDM). Demagnetization curves at three different temperatures (25°C, 100°C, and 160°C) were recorded using a Vibrating Sample Magnetometer (VSM). Crystallographic alignment

distributions are evaluated by X-ray diffraction and microstructure investigations are determined by Scanning Electron Microscope (SEM).

5.2 Results and Discussion

Microstructural and magnetic properties of hot-deformed magnets vary with hot-deformation parameters. Table 5-1 lists the hot-deformation temperature, strain rate and maximum stress for each sample during the hot-deformation process. The following two sections will discuss the influence of hot-deformation parameters on microstructural and magnetic properties of the magnets.

Table 5-1Hot deformation parameters for each sample

Sample	Hot-deformation Temperature	Maximum Stress (σ)/MPa	Strain rate ($\dot{\varepsilon}$)
M1	680°C	63±4	$0.020s^{-1}$
M2	750°C	42±4	$0.014s^{-1}$
M3	800°C	34±4	$0.017s^{-1}$
M4	850°C	33±4	$0.017s^{-1}$
M5	900°C	20±4	$0.020s^{-1}$

5.2.1 Hot Deformation Parameters on Microstructural Properties of Magnets

Higher deformation temperatures usually lead to magnets consisting of larger grains. Figure 5-1and Figure 5-2 shows the cross-sectional SEM images and distribution of grain dimensions for each sample. Figure 5-3 summarizes the effect of hot-deformation temperature on the average grain size of the magnets. When the temperature reaches ~900°C, the dimensions of crystallites in the magnet are $\sim 1100nm \times 200nm$, which is large enough to support multiple magnetic domains. When the deformation temperature decreases to ~680°C, the size of each crystallite decreases to $\sim 230nm \times 90nm$, which is comparable to the single domain size of $Nd_2Fe_{14}B$ material (~300nm). The results show that the low temperature prevents the growth of grains and it also decreases the aspect ratio from ~5.5 to ~2.6. Usually, stripes of large grains with dimension of ~1 μm are periodically distributed in the hot-deformed magnets, which is shown in Figure 5-4 (a) and (b). However, when the hot-deformation temperature decreases to ~680°C, an interesting phenomenon occurs where the stripes of large grains disappear and only grains that are small enough to support single domains remain (shown in Figure 5-4 (c)).

Figure 5-5 illustrates the X-ray diffraction data of all the samples along with the degree of crystallographic alignment for each sample, calculated by the method described in Chapter 3. The degree of crystallographic alignment ranges from 32vol% to 59vol%. The low alignment of sample M5 can be explained by the hot-deformation mechanism discussed in the next paragraph. In addition, literature [23, 38] pointed out that the crystallographic alignment is related to the deformation ratio. Although the deformation ratio of each sample is designed to be kept constant (~70%), experimental results show that the actual

deformation ratio varies from 67% to 85% and that there is no significant linear relation between the deformation ratio and the degree of crystallographic alignment.

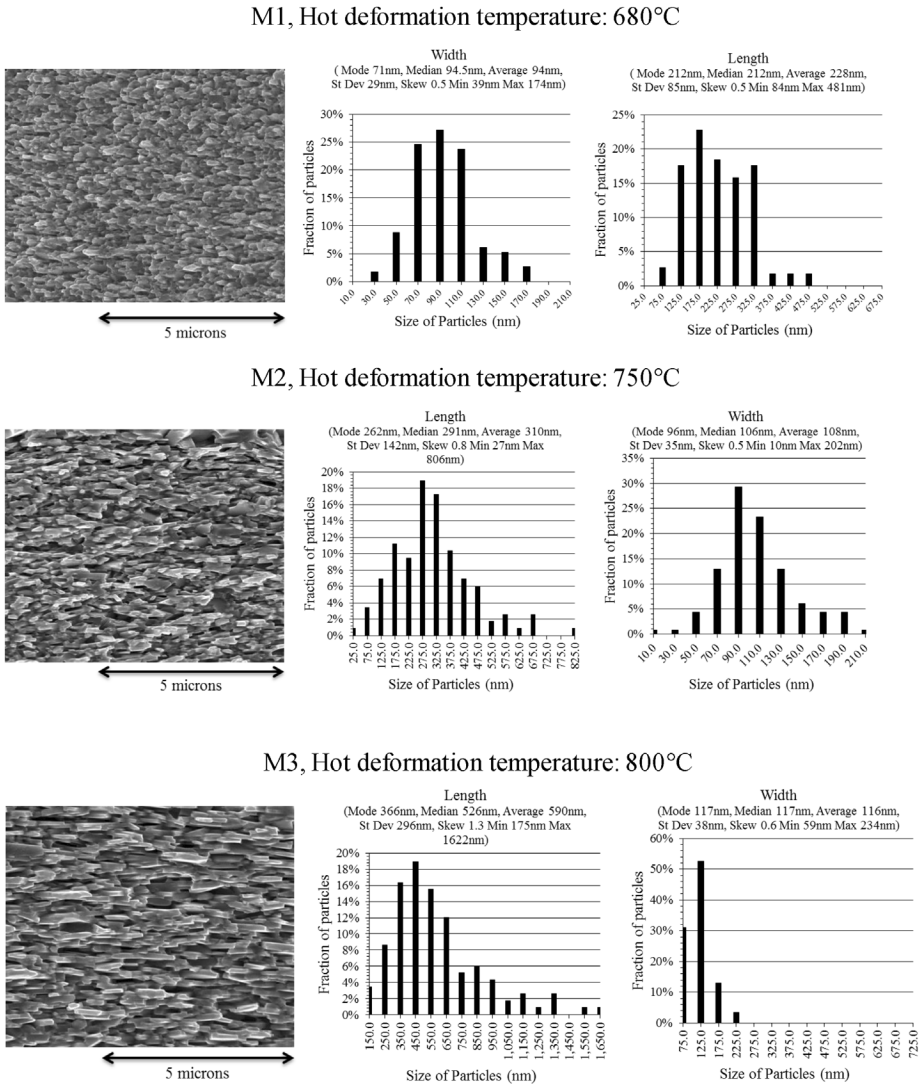

Figure 5-1 The cross-sectional SEM images and grain size distributions of the magnets hot-deformed at 680°C, 750°C and 800°C.

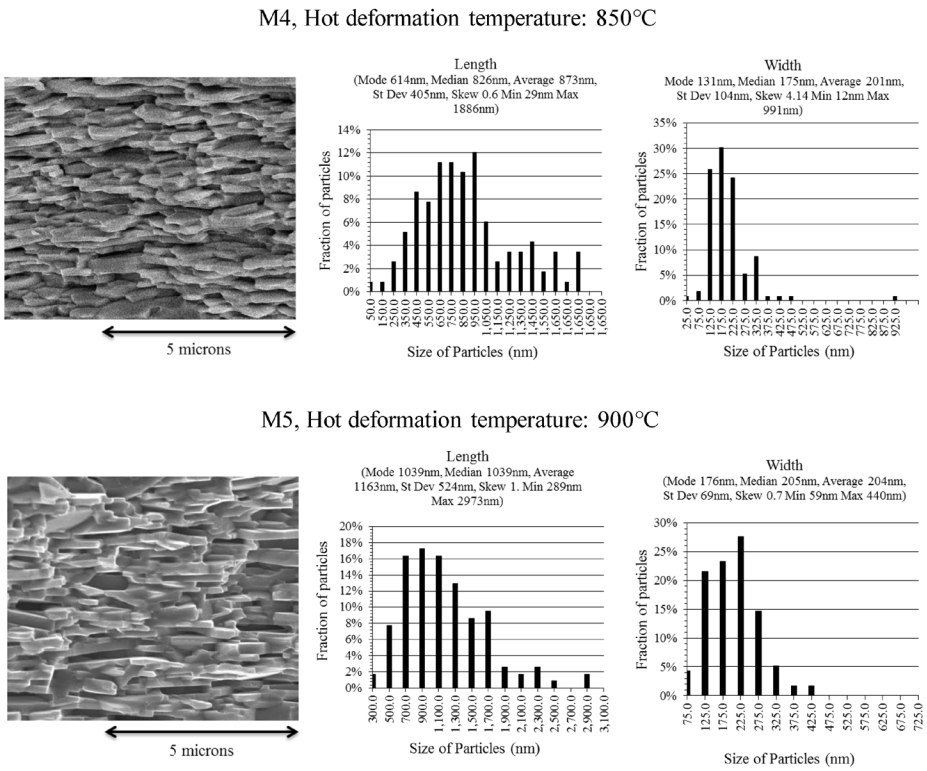

Figure 5-2 The cross-sectional SEM images and grain size distributions of the magnets hot-deformed at 850°C and 900°C.

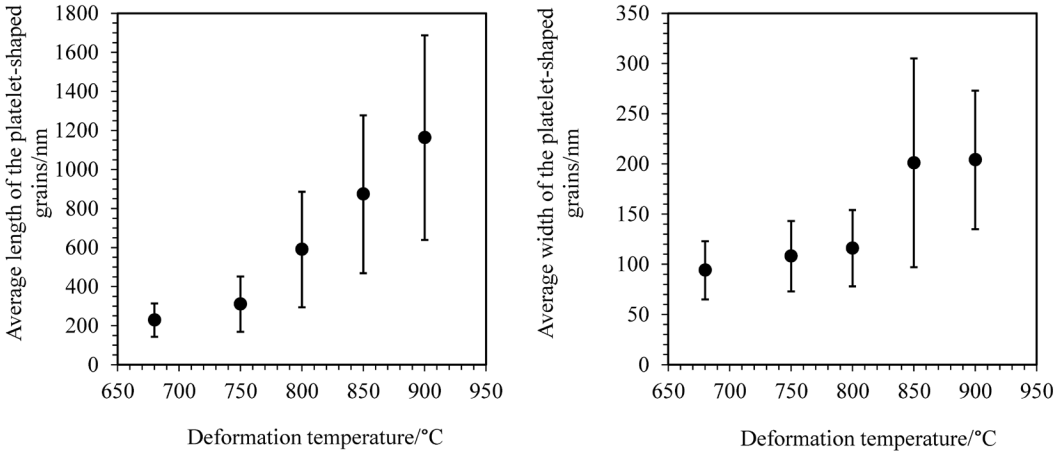

Figure 5-3 The dependence of grain dimensions of hot-deformed magnets on temperature.

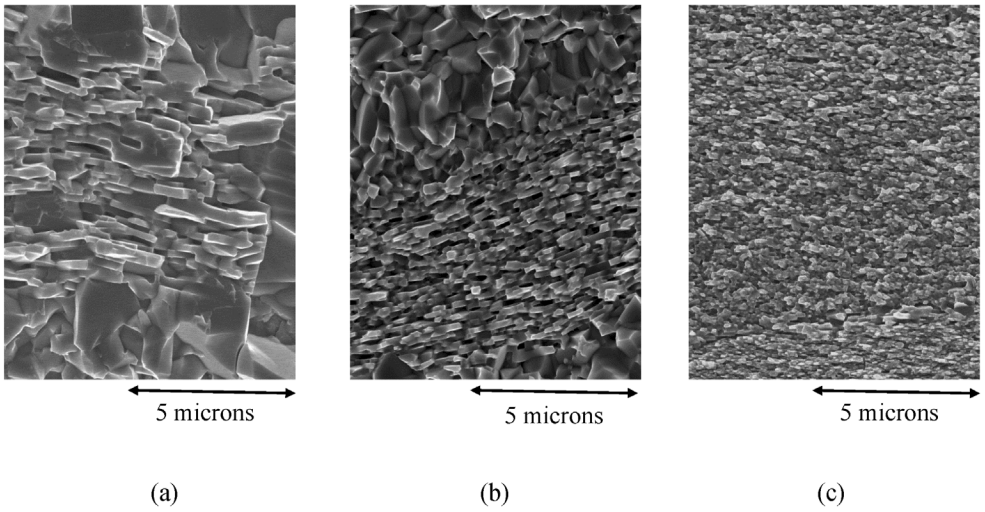

Figure 5-4 The cross-sectional SEM images of the magnets hot-deformed at (a) 900°C, 16MPa (b) 800°C, 34MPa and (c) 680°C, 63MPa.

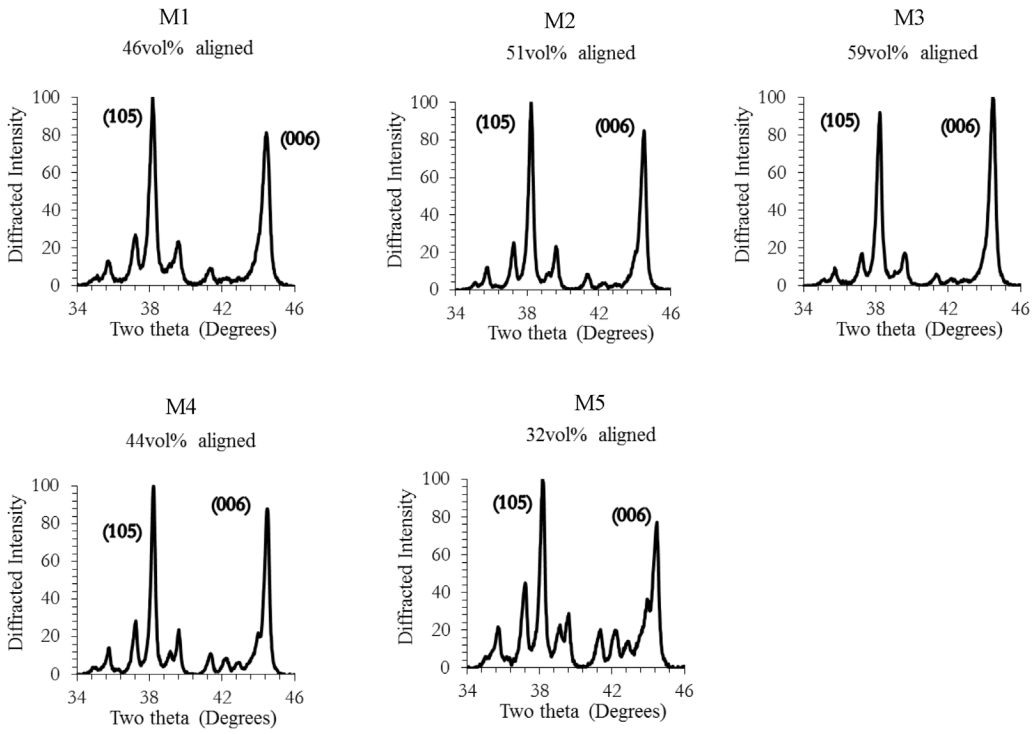

Figure 5-5 X-ray diffraction data of magnets hot-deformed at different temperature.

According to Li's model introduced in Chapter 2, $\sigma \propto \exp(\frac{\Delta G_{vis}}{2RT})$ and the experimental results show that $\dot{\varepsilon} \propto \sigma^{2.5}$ [39]. The crystallographic alignment for anisotropic hot-deformed magnets depends on the solution–precipitation–creep mechanism, and the general model for the creep mechanism is expressed as:

$$\dot{\varepsilon} = A_{creep}\sigma^{n} \exp(-\frac{\Delta Q}{RT}) \tag{5.1}$$

In this equation, A_{creep} is a constant that depends on the materials and creep mechanism and ΔQ is the activation energy for the creep mechanism. Combing Li's model and the general equation for creep mechanism[39]:

$$\dot{\varepsilon} = A_{creep}\sigma^{2.5}\exp(-\frac{\Delta G_{vis}}{RT}) \tag{5.2}$$

When the strain rate $\dot{\varepsilon}$ is constant, then $\ln\sigma$ is a linear function of $1/T$:

$$\ln\sigma = \frac{\Delta G_{vis}}{2.5R}\cdot\frac{1}{T} + \frac{1}{2.5}\cdot(\ln\dot{\varepsilon} - \ln A_{creep}) \tag{5.3}$$

This relationship shows that lower temperatures will results in a higher stress acting on the magnet when the strain rate is kept constant. The low comparative crystallographic alignment of M5 is due to the low hot-deformation stress caused by the relatively high temperature (~900°C).

Figure 5-6 shows the relationship between the stress and temperature, where the y-axis is the natural logarithm of the stress and x-axis is the reciprocal temperature (1000/T). The linear regression line is fitted by the least square method and it gives that:

$$\ln\sigma = (5.29\pm0.81)\times\frac{1000}{T} - (1.41\pm0.77) \tag{5.4}$$

Based on the regression results, the constant $\ln A_{creep} = -0.56\pm1.91 s^{-1}MPa^{-2.5}$ and the activation energy of viscosity ΔG_{vis} for this material is $110\pm17 kJ/mol$, which is close to the value of Nd-Fe-Co-B alloys estimated in the literature[39], $115 kJ/mol$. Higher melting temperature usually results in high activation energy of viscous flow[40]. The melting temperature for pure Fe is ~1800K, which is higher than that of Nd-Fe alloy. However, the activation energy of viscous flow (ΔG_{vis}) for pure Fe is $\sim 41.4 kJ/mol$ [40].

The estimated activation energy of viscous flow for the eutectic Nd-Fe phase is much higher than that for pure Fe, even though the melting temperature is lower. This indicates that the creep model does not accurately estimate the activation energy of viscous flow for the eutectic phase.

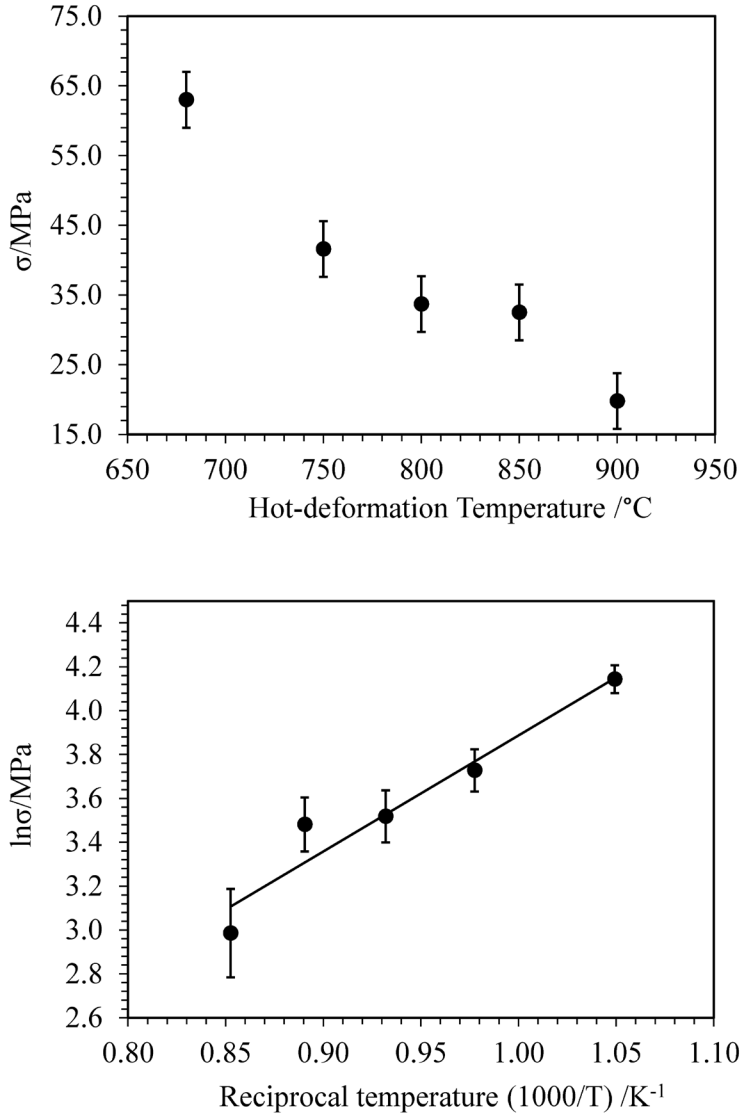

Figure 5-6 The relationship between maximum stress and hot-deformation temperature.

5.2.2 Hot Deformation Parameters on Magnetic Properties of Magnets

Figure 5-7 shows the temperature-dependent demagnetization curves for each sample. The effect of hot-deformation temperature on coercivity and remanence at three different temperatures is illustrated in Figure 5-8. The room temperature coercivity of the magnets increases from 1.56T to 2.11T and the remanence increases from 1.15T to 1.22T when the hot-deformation temperature decreases from 900°C to 680°C. The improvement of coercivity may be due to the refinement of grain size, which results from the low hot-deformation temperature. This also leads to high remanences of the magnets because the remanence depends on the crystallographic alignment. The driving force for the alignment in the hot-deformation process is proportional to stress, and at lower temperatures, a higher stress is required to achieve the same strain rate. Therefore, lowering the hot-deformation temperature is predicted to improve the crystallographic alignment of magnets.

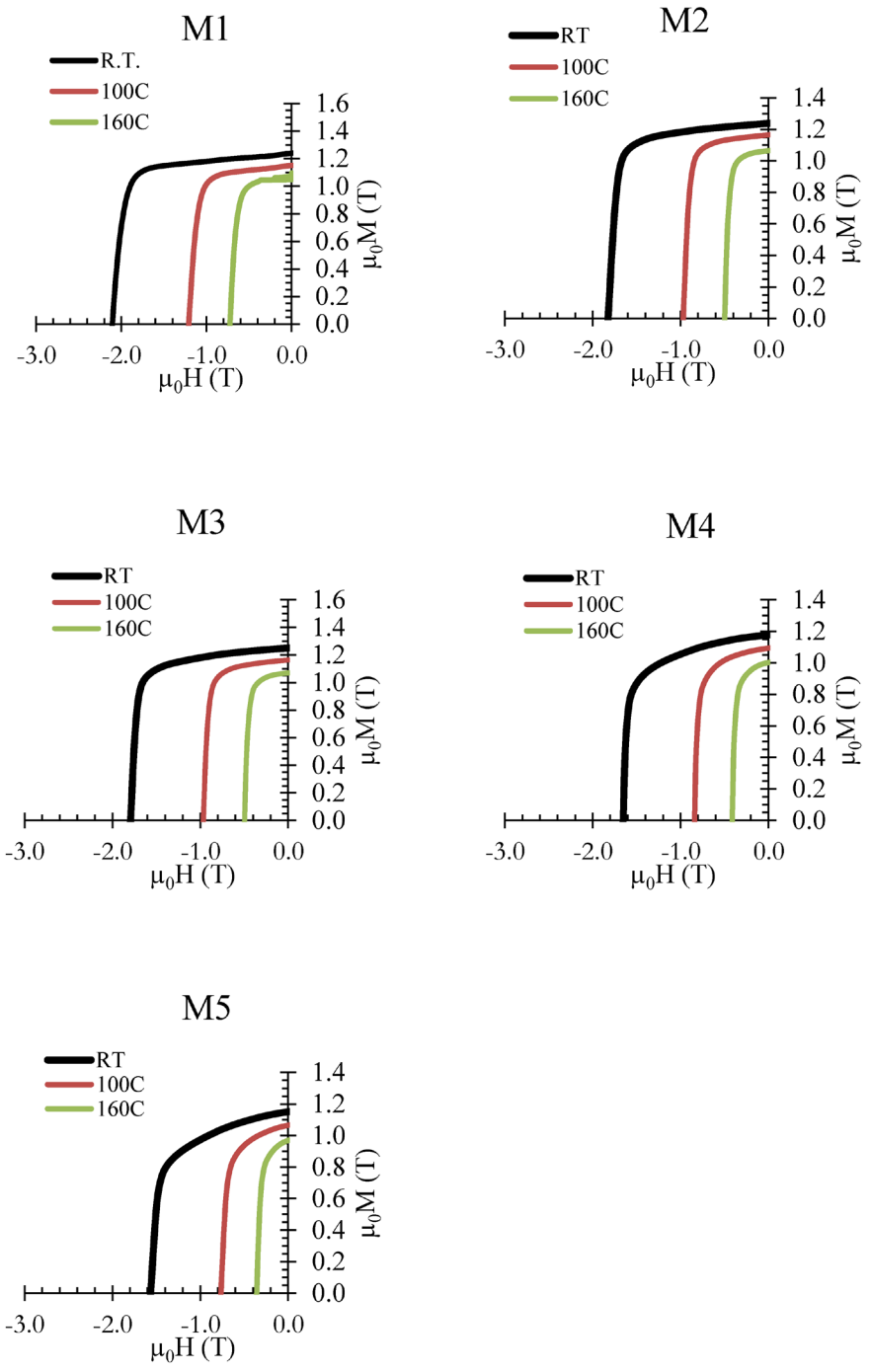

Figure 5-7 Demagnetization curves of magnets hot-deformed at different temperatures.

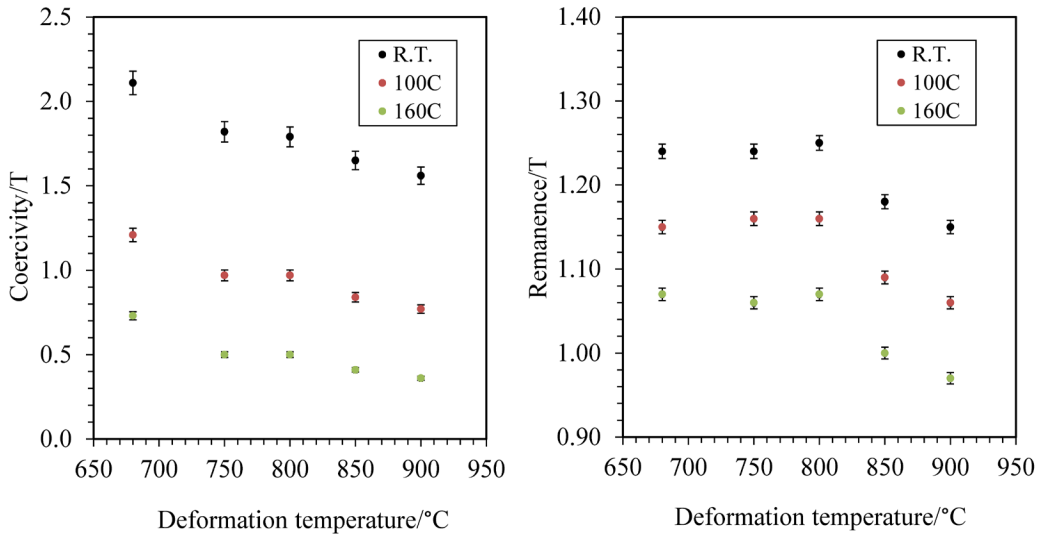

Figure 5-8 The dependence of coercivity and remanence on hot-deformation temperature.

5.3 Conclusions

It has been shown that bulk $RE_2TM_{14}B$ magnets consisting of crystallites which are small enough to support single domains can be manufactured by hot-deformation processing. The effect of hot-deformation parameters on the microstructural and magnetic properties of magnets are analyzed. The regression results indicate that the solution-precipitation creep model does not accurately estimate the activation energy of viscous flow for the eutectic phase. The VSM results show that the coercivity of the magnets decreases with an increase in hot-deformation temperature. The coercivity and remanence of hot-deformed magnets can be increased to 2.11T and 1.22T, respectively, at room temperature when they are hot-deformed at ~680°C.

Chapter 6

Effect of Modifying Inter-granular Phase on Microstructural and Magnetic Properties of $RE_2TM_{14}B$ Magnets

The work done in this chapter is to resolve Tasks #3, #4 and #5. The first goal is to examine whether the submicron crystallites in the magnets can be aligned via hot-deformation processing with a modified intergranular phase. The second goal is to investigate whether the coercivity of hot-deformed $RE_2TM_{14}B$ magnets can be increased to satisfy the requirement for traction motors used in hybrid and electric vehicles when the ferromagnetic inter-granular phase (Nd-Fe phase) is diluted by a non-magnetic phase (Nd-Cu phase). Experimental results show that the developed hot-deformation process can produce bulk magnets with the microstructural features described above, and that these magnets, which

only contain ~2.5wt% Dy, have similar coercivity to commercially sintered magnets containing ~7wt% Dy. The demagnetization behaviors are analyzed based on a phenomenological model, and the effect of the modified intergranular phase on the magnetic interaction between neighboring grains is discussed.

6.1 Experimental Design

Two types of hot-deformed magnets are examined in this chapter. The first type consists entirely of the commercial ribbon particles described in Chapter 5. The ribbon particle has a composition of 2.6wt% Dy, 7.0wt%Pr, 20.9wt% Nd, 0.9wt%B, 4.0wt% Co, 0.5wt%Ga, and 64.1wt% Fe. The second type differs from the first in that 5.0wt% of the magnet consists of a rapidly solidified Dy-free 70at%Nd, 30at%Cu alloy powder that is mixed with the commercial ribbon particles prior to consolidation. The $Nd_{0.7}Cu_{0.3}$ ribbons are obtained by melt-spinning onto a large copper wheel within an argon atmosphere. The linear speed of the wheel is 30m/s. The ribbons are then crushed into powders with an average particle size of approximately 300 microns. As discussed in Chapter 5, the optimal hot-deformation temperature is ~680°C. All of the magnets analyzed in this chapter are hot-deformed at this temperature and the strain rates are kept between $0.013s^{-1}$ to $0.020s^{-1}$. These two types of magnets are referred to as A0, B0, and C0; and A5, B5, and C5 respectively. In order to analyze the cause of the increase in coercivity according to the phenomenological model, demagnetization curves of each sample are measured at five different temperatures (25°C, 70°C, 100°C, 130°C, and 160°C) by using a Vibrating Sample Magnetometer (VSM).

6.2 Results and Discussion

6.2.1 Microstructural Properties of Hot-deformed Magnets with Modified Intergranular Phase

Whether a non-Fe-containing eutectic phase can serve as a media to dissolve, transport, and re-precipitate $Nd_2Fe_{14}B$ grains may influence the alignment of the magnets. It has been shown that the required selective dissolution and reprecipitation mechanism operates during hot deformation even when the Nd-Fe phase is diluted by Nd-Cu alloy. The X-ray diffraction data of these two types of hot-deformed magnets shown in Figure 6-1 indicates that the modification of the intergranular phase does not weaken the crystallographic alignment of the magnets. The comparison between the microstructures of hot-deformed magnets with and without modified intergranular phase, shown in Figure 6-2, also illustrates that both bulk magnets exhibit the aligned platelet-shaped structure, which is characteristic of selective dissolution and precipitation. For all the 6 hot-deformed magnets, the mean and standard deviation of the size distribution in crystallite dimensions along the magnetically easy direction vary from $90nm \pm 30nm$ to $60nm \pm 20nm$; the mean and standard deviation in the dimensions of the crystallites for the direction perpendicular to the magnetically easy direction vary from $230nm \pm 80nm$ to $180nm \pm 70nm$. These dimensions are on the order of the critical size for a single domain (~300nm). It can be concluded that both hot-deformed magnets, with and without diluting the intergranular phase by $Nd_{0.7}Cu_{0.3}$ alloy, consist of submicron grains which are small enough that they can only support single domains.

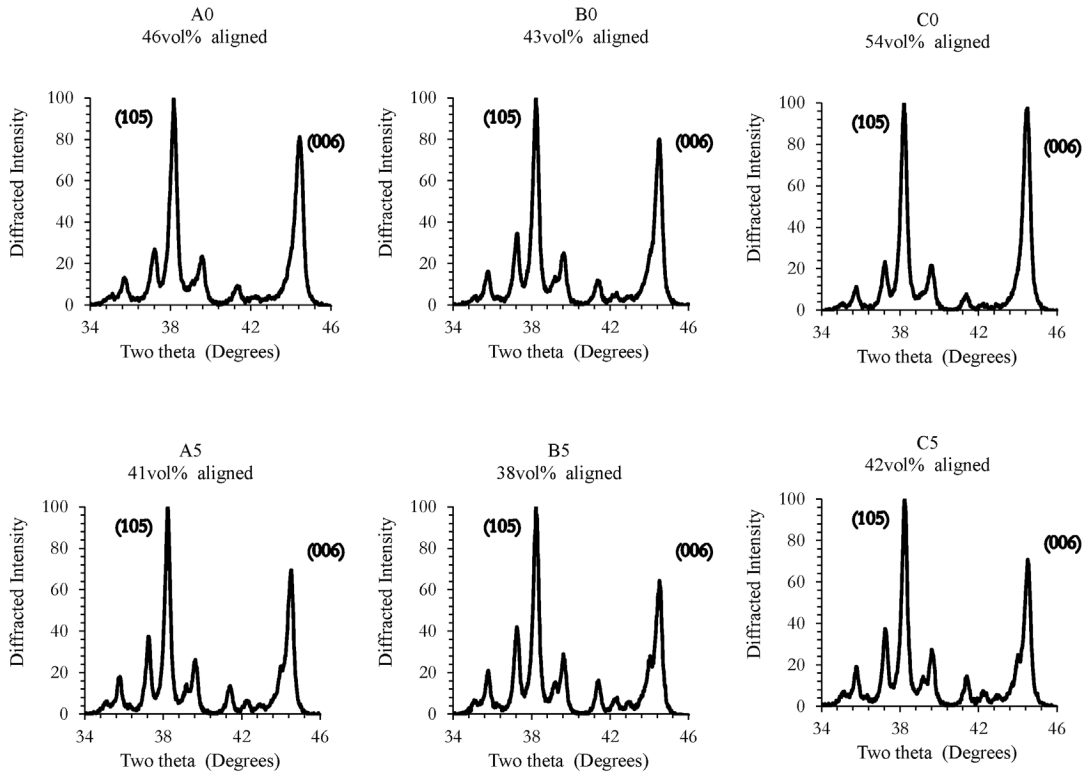

Figure 6-1 X-ray diffraction data for hot-deformed magnets containing 0wt% and 5wt% $Nd_{0.7}Cu_{0.3}$ additives.

A0

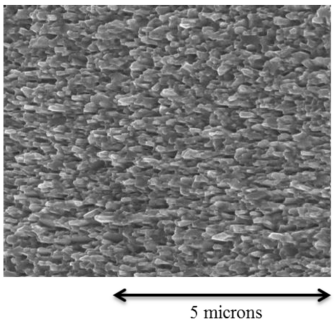
5 microns

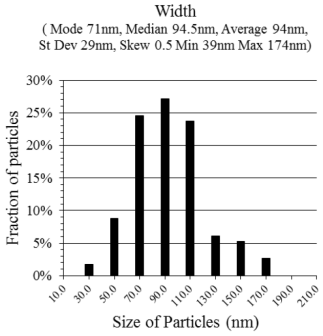
Width
(Mode 71nm, Median 94.5nm, Average 94nm,
St Dev 29nm, Skew 0.5 Min 39nm Max 174nm)
Fraction of particles
Size of Particles (nm)

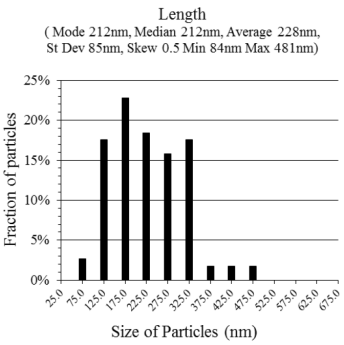
Length
(Mode 212nm, Median 212nm, Average 228nm,
St Dev 85nm, Skew 0.5 Min 84nm Max 481nm)
Fraction of particles
Size of Particles (nm)

B0

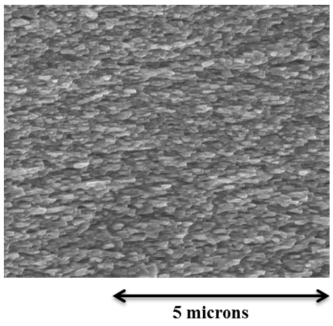
5 microns

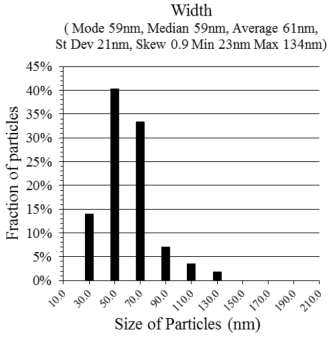
Width
(Mode 59nm, Median 59nm, Average 61nm,
St Dev 21nm, Skew 0.9 Min 23nm Max 134nm)
Fraction of particles
Size of Particles (nm)

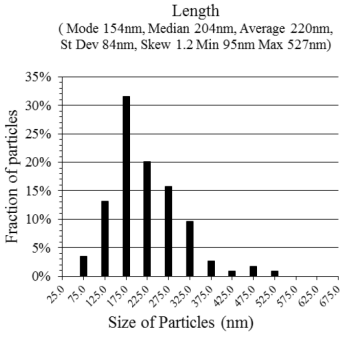
Length
(Mode 154nm, Median 204nm, Average 220nm,
St Dev 84nm, Skew 1.2 Min 95nm Max 527nm)
Fraction of particles
Size of Particles (nm)

C0

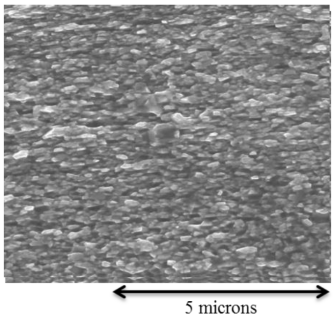
5 microns

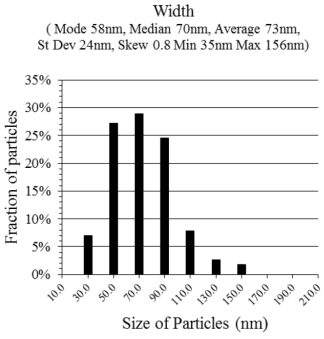
Width
(Mode 58nm, Median 70nm, Average 73nm,
St Dev 24nm, Skew 0.8 Min 35nm Max 156nm)
Fraction of particles
Size of Particles (nm)

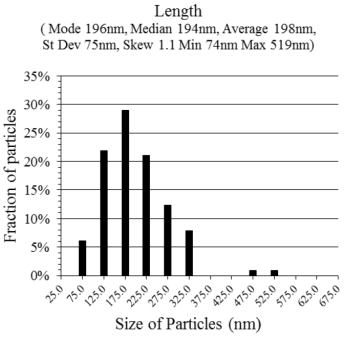
Length
(Mode 196nm, Median 194nm, Average 198nm,
St Dev 75nm, Skew 1.1 Min 74nm Max 519nm)
Fraction of particles
Size of Particles (nm)

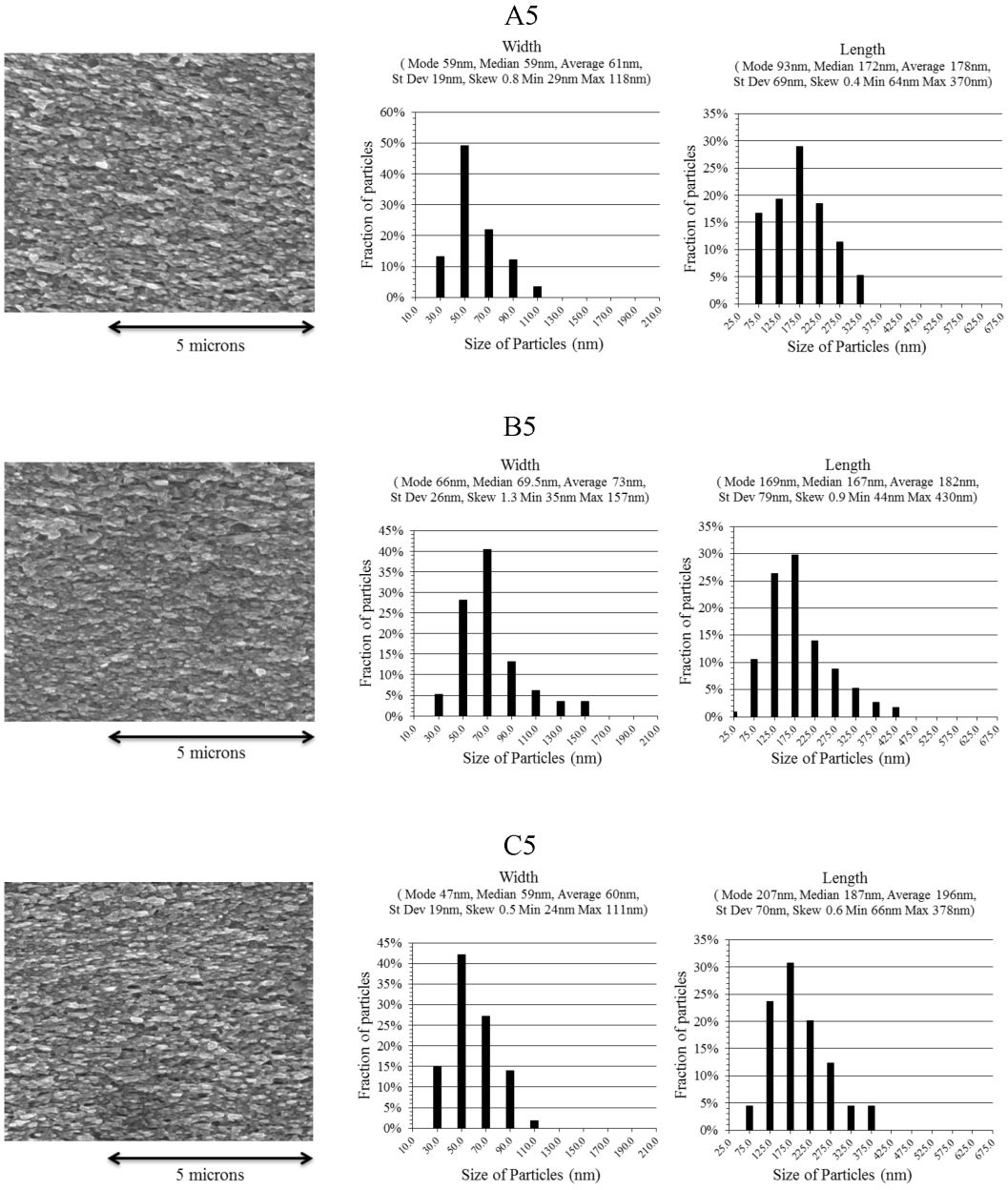

Figure 6-2 Cross-sectional SEM images and grain size distribution for hot-deformed magnets containing 0wt% and 5wt% $Nd_{0.7}Cu_{0.3}$ additives.

6.2.2 Magnetic Properties of Developed Hot-deformed Magnets

The developed hot-deformed magnets with reduced amounts of Dy (~2.5wt% Dy) have comparable magnetic properties to the Dy-diffused sintered magnets containing ~4wt% Dy and non-Dy-diffused sintered magnet containing ~7wt% Dy. Traction motors of electric and hybrid vehicles require both the coercivity of their magnets to be ~0.9T and remanence to be ~1T at 160°C. Figure 6-3 shows the temperature-dependent demagnetization curves of these two types of hot-deformed magnets (A0, B0, and C0; and A5, B5, and C5) and Figure 6-4 plots the temperature dependent coercivity and remanence for these six magnets. At an elevated temperature of 160°C, the coercivity and remanence of hot-deformed magnets with diluted intergranular phase are 0.88T and 0.99T, respectively, which satisfy the requirement for the traction motors of electric and hybrid vehicles. A visualized comparisons of magnetic properties between hot-deformed magnets with modified intergranular phase and commercial sintered magnets at 160°C is shown in Figure 6-5. The dashed line with $\mu_0 H_C = 0.9T$ is the requirement of electric and hybrid vehicles application. The red dots present the magnetic properties of hot-deformed magnets with diluted grain boundary phase. As described in Chapter 4, the amount of Dy in the magnets can be decreased from ~7wt% to ~4wt% after a complex and expensive Dy diffusion process. Hot-deformed magnets with modified intergranular phase and ~2.5wt% Dy have approximately the same coercivity. Additionally, compared with the sintering approach, hot-deformation eliminates hydrogen embrittlement and the need for a strong magnetic field for alignment. Cold compaction and high temperature sintering is replaced with consolidation followed by deformation under moderate pressure at lower temperatures (~680°C). Although the remanence of the hot-deformed magnets is slightly lower than that

of the sintered magnets, they still satisfy the requirements for the application of traction motors in electric and hybrid vehicles.

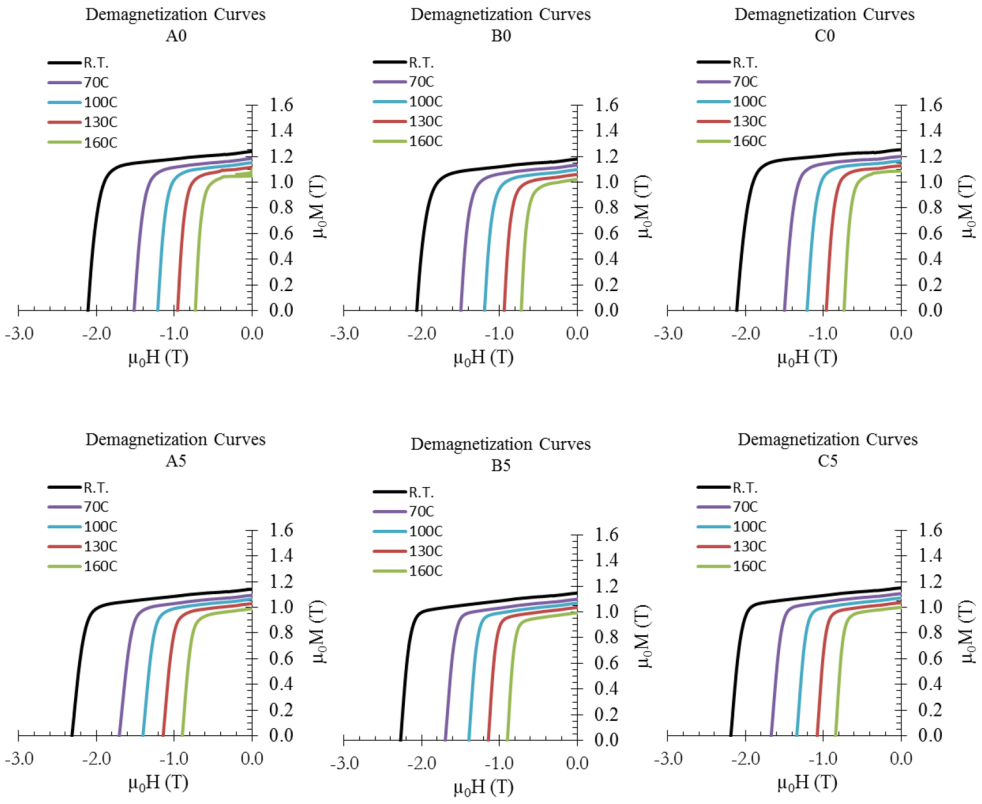

Figure 6-3 Temperature-dependent demagnetization curves for six hot-deformed magnets.

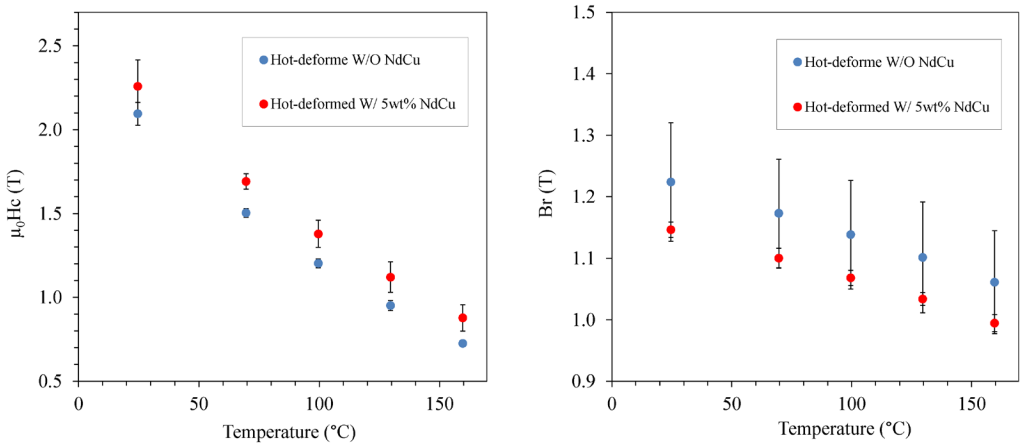

Figure 6-4 Temperature dependence of coercivity and remanence for hot-deformed magnets without $Nd_{0.7}Cu_{0.3}$ additives, hot-deformed magnets with 5wt% $Nd_{0.7}Cu_{0.3}$ additives.

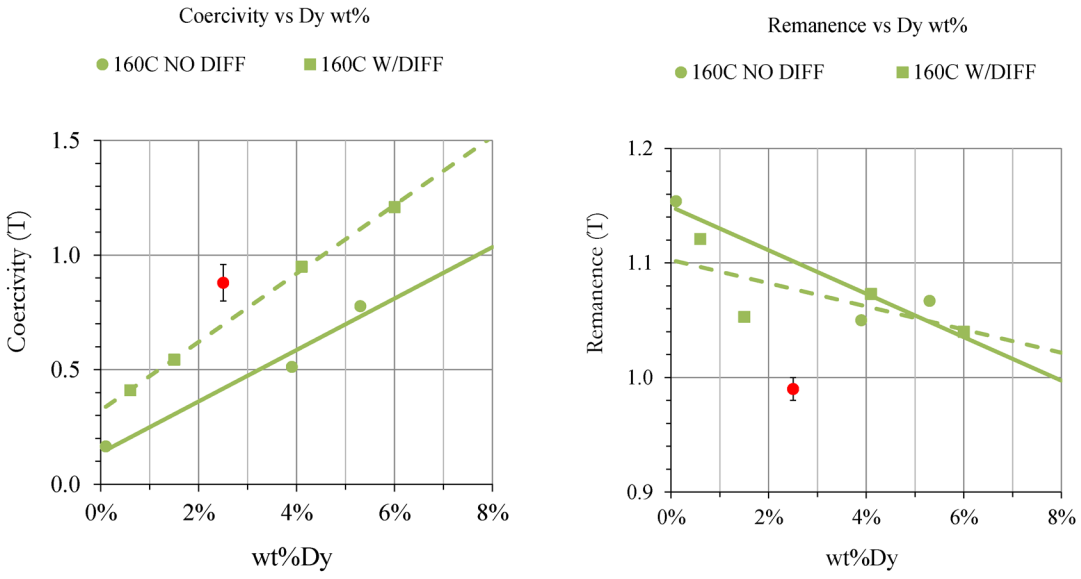

Figure 6-5 Comparisons of magnetic properties between sintered and hot-deformed magnets.

6.2.3 Impact of Diluting Intergranular Phase on Magnetic Properties of Hot-deformed Magnets

As shown in Figure 6-4, the coercivity of hot-deformed magnets increases from 2.09T to 2.26T and remanence decreases from 1.22T to 1.15T at room temperature by adding 5wt% of the non-ferromagnetic $Nd_{0.7}Cu_{0.3}$ alloy. The decrease in remanence may result from the decreased amount of effective magnetic hard phase. Based on the stoichiometry of the materials, the weight percent of magnetic hard phase and intergranular phase can be calculated. For A0, B0 and C0, they consist of 93wt% magnetic hard phase ($[Dy_{0.08}Pr_{0.24}Nd_{0.68}]_2[Fe_{0.94}Co_{0.06}]_{14}B$) and 7wt% intergranular phase ($[Dy_{0.08}Pr_{0.24}Nd_{0.68}]_{0.7}[Fe_{0.94}Co_{0.06}]_{0.3}$). Samples A5, B5 and C5 have 88wt% magnetic hard phase ($[Dy_{0.08}Pr_{0.24}Nd_{0.68}]_2[Fe_{0.94}Co_{0.06}]_{14}B$), 7wt% grain boundary phase ($[Dy_{0.08}Pr_{0.24}Nd_{0.68}]_{0.7}[Fe_{0.94}Co_{0.06}]_{0.3}$) and 5wt% $Nd_{0.7}Cu_{0.3}$. The density of commercial ribbon particles is 7.625±0.002g/cm^3 and it is 6.993±0.004g/cm^3 for $Nd_{0.7}Cu_{0.3}$ ribbons. Then, an assumption is made that the volume percent of each phase is approximated by the weight percent. The volume percent of grain boundary phase increases from 7% to 12% when 5wt% of $Nd_{0.7}Cu_{0.3}$ alloy is added to the grain boundary region. As a result, the volume percent of hard phase decreases from 93% to 88% and ~36% of the grain boundary phase are diluted by this non-ferromagnetic $Nd_{0.7}Cu_{0.3}$ alloy. The stoichiometry of the grain boundary phase changes from $[Dy_{0.08}Pr_{0.24}Nd_{0.68}]_{0.7}[Fe_{0.94}Co_{0.06}]_{0.3}$ to $[Dy_{0.08}Pr_{0.24}Nd_{0.68}]_{0.7}[Fe_{0.57}Cu_{0.37}Co_{0.06}]_{0.3}$, and 40% of the Fe is diluted by Cu. The ratio of hard phase between magnets with and without adding $Nd_{0.7}Cu_{0.3}$ alloy is $\frac{93\%}{88\%} = 1.06$ and the ratio of room temperature remanence between magnets with and without adding

$Nd_{0.7}Cu_{0.3}$ alloy is $\frac{1.22T}{1.15T} = 1.06$. The results show that the decrease of remanence is potentially caused by adding additional non-ferromagnetic $Nd_{0.7}Cu_{0.3}$ alloy.

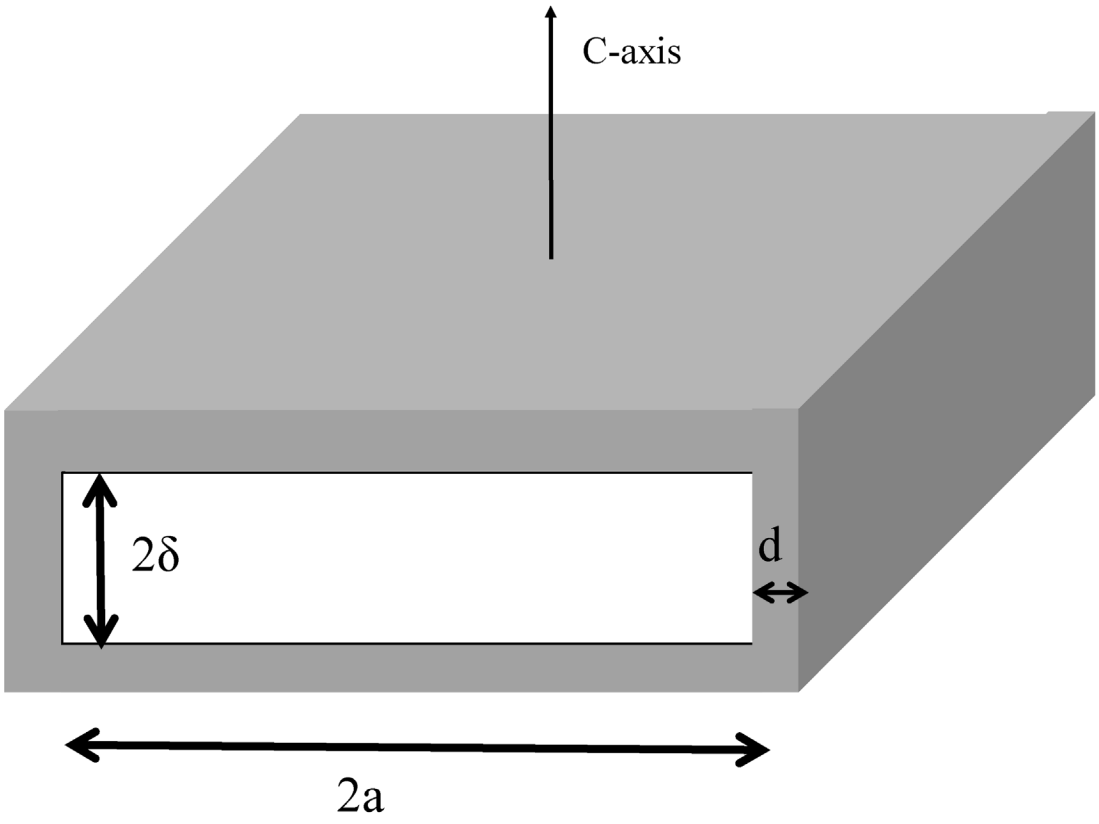

Figure 6-6 A single platelet-shaped grain (2a × 2a × 2δ) is surrounded by a grain boundary phase of thickness 2d.

Figure 6-6 illustrates that the platelet-shaped grain which is surrounded by a thin layer of grain boundary phase. The dimensions of the platelet-shaped grain are $2a \times 2a \times 2\delta$, and the thickness of the grain boundary phase is $2d$. Thus the volume percent of grain boundary phase can be estimated as:

$$Vol\% = \frac{(2a+2d)^2 \times (2\delta+2d) - 8a^2\delta}{(2a+2d)^2 \times (2\delta+2d)} \tag{6.1}$$

Submitting the dimension of crystallites and volume percent of grain boundary phase into Equation (6.1), the grain boundary thickness ($2d$) increases from ~3nm to ~5nm. The grain boundary thickness of the hot-deformed magnets in this study without adding $Nd_{0.7}Cu_{0.3}$ is in agreement with experimental measurements from literature [41].

As described in Chapter 2, the mechanisms that reduce the coercivity from the anisotropy field H_K can be characterized by the following formula:

$$\mu_0 H_C = \alpha\mu_0 H_K - N_{eff}\mu_0 M_S \tag{6.2}$$

In this expression, M_S is the saturation magnetization for the magnetic hard phase [13, 31, 42-44]. The values of α and N_{eff} can be determined by firstly measuring the H_C of a particular material at different temperatures. Then, α and N_{eff} can be extracted from the slope and intercept of a plot of H_C/M_S vs H_K/M_S if H_K and M_S are known. The estimation of H_K and M_S for $[Dy_{0.08}Pr_{0.24}Nd_{0.68}]_2[Fe_{0.94}Co_{0.06}]_{14}B$ is made based on the extension of Vegard's law described in Chapter 2. The calculated M_S and H_K values of this material at different temperatures are listed in Table 6-1. The dependence of H_C/M_S on H_K/M_S for hot-deformed magnets, with and without $Nd_{0.7}Cu_{0.3}$ additives, are plotted from room temperature to 160°C, illustrated in Figure 6-7. The fitted values of parameters α and N_{eff} for each sample are calculated based on the least square regression method. Since there are only three duplicate samples for each experiment, the 95% confidence intervals for the mean of α and N_{eff} are calculated based on the t-distribution instead of assuming the sample follows the normal distribution:

$$\bar{x} \pm t \times (\frac{\sigma}{\sqrt{n}}) \tag{6.3}$$

In this equation, t is a coefficient dependent on the degree of freedom (n-1), σ is the standard deviation based on the experimental data and n is the sample size (n=3). The resulting values for α and N_{eff} shown in Table 6-2.

Table 6-1 Calculated value of M_S, H_K for $[Dy_{0.08}Pr_{0.24}Nd_{0.68}]_2[Fe_{0.94}Co_{0.06}]_{14}B$ and experimental value of M_S, H_K for $Nd_2Fe_{14}B$

	$[Dy_{0.08}Pr_{0.24}Nd_{0.68}]_2[Fe_{0.94}Co_{0.06}]_{14}B$		**$Nd_2Fe_{14}B$**	
Temperature	M_S/Tesla	H_K/Tesla	M_S/Tesla	H_K/Tesla
25°C	1.53	7.78	1.61	6.56
70°C	1.50	6.82	1.53	6.03
100°C	1.47	6.15	1.46	5.63
130°C	1.41	5.45	1.41	5.09
160°C	1.34	4.75	1.32	4.42

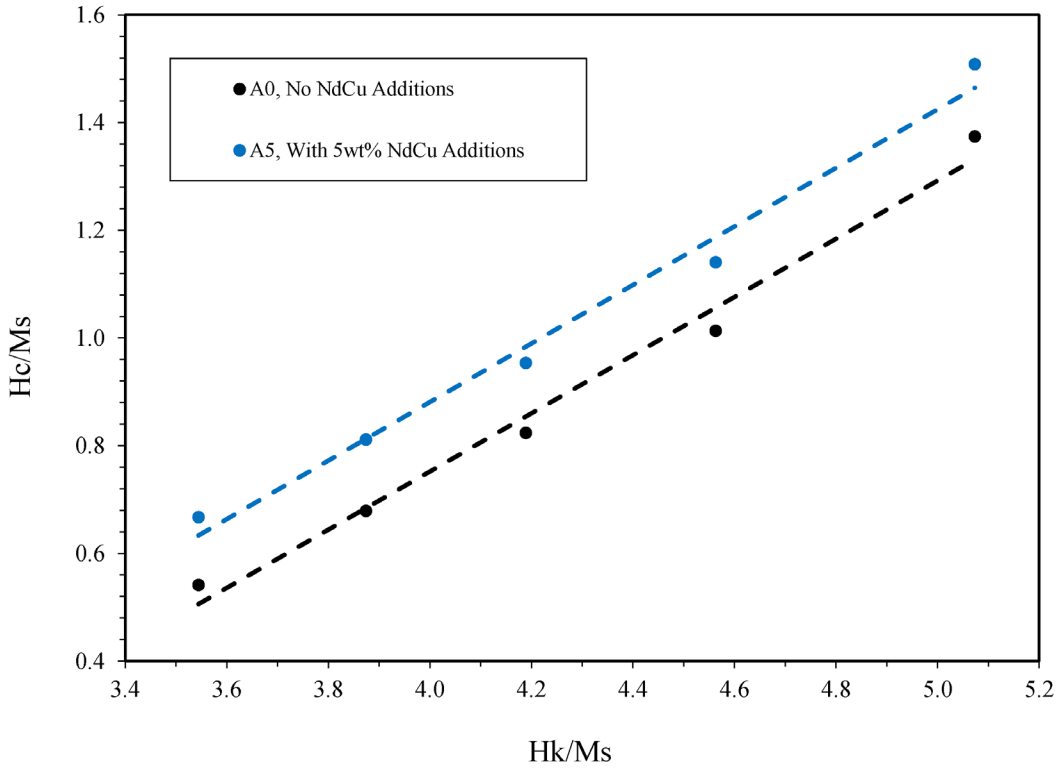

Figure 6-7 The dependence of H_C/M_S on H_K/M_S for hot-deformed magnet with 5wt% $Nd_{0.7}Cu_{0.3}$ additives (blue line) and without $Nd_{0.7}Cu_{0.3}$ additives (black line) at different temperatures.

Table 6-2 Values of parameters α and N_{eff} for hot-deformed $Nd_2Fe_{14}B$-based magnetic materials.

Materials	**α**	**N_{eff}**
Hot-deformed magnets without $Nd_{0.7}Cu_{0.3}$ additives in this work	0.54±0.02	1.39±0.05
Hot-deformed magnets with 5wt% $Nd_{0.7}Cu_{0.3}$ additives in this work	0.53±0.03	1.26±0.08

The regression data clearly shows that there is no significant change in α, while N_{eff} decreases from 1.39 to 1.26 when 5 wt% of $Nd_{0.7}Cu_{0.3}$ alloy is added. The results of the phenomenological model show that adding 5 wt% $Nd_{0.7}Cu_{0.3}$ alloy into the grain boundary phase does not influence the exchange coupling between the neighboring grains but that it does decrease the internal stray field. The internal field of a single grain can be determined if the distribution of magnetization $\vec{M}$ inside the grain is known. If there is no free current inside the grains, the stray field can be determined from a scalar potential Ψ :

$$\vec{H}_S = -\nabla\Psi \tag{6.4}$$

According to Maxwell's equation $\nabla \cdot \vec{B} = 0$, and $\vec{B} = \mu_0(\vec{M} + \vec{H})$, thus

$$\nabla \cdot \vec{H}_S = -\nabla \cdot \vec{M} \tag{6.5}$$

Similar to the bound charge in the electric polarized object, the effective magnetic charge density can be given by:

$$\rho = -\nabla \cdot \vec{M} \tag{6.6}$$

Combining Equation (6.4), (6.5) and (6.6), it gives that:

$$\nabla^2\Psi = -\rho \tag{6.7}$$

The scalar potential Ψ can be obtained by solving this Poisson's equation:

$$\Psi(\vec{r}) = \frac{1}{4\pi}\int \frac{\rho(\vec{r}\,')\cdot d\tau'}{|\vec{r} - \vec{r}\,'|} \tag{6.8}$$

and the stray field can be calculated based on Equation (6.4). In the hot-deformed magnets, it is assumed that the platelet-shaped grains with dimensions of $2a \times 2a \times 2\delta$ are uniformly magnetized in the z direction ($\vec{M} = M_S\hat{z}$), which is shown in Figure 6-8. The uniform

magnetization $\vec{M}$ creates surface charge density σ without creating volume charge density ρ. This surface charge density is expressed as follows:

$$\sigma = \vec{M} \cdot \hat{n} \tag{6.9}$$

This gives a scalar potential Ψ of:

$$\Psi(\vec{r}) = \frac{1}{4\pi} \int \frac{\sigma(\vec{r}\,') \cdot df'}{|\vec{r} - \vec{r}\,'|} \tag{6.10}$$

Both positive surface charge at $\vec{r} = (x', y', \delta)$ and negative surface charge at $\vec{r} = (x'', y'', -\delta)$ should be considered to calculate the scalar potential Ψ. According to Kronmüller's work[17], the most probable occurrence of the nucleation of reverse domains usually occurs in the region where the anisotropy constant K_1 is low such as the inter-granular phase, in the vicinity of non-magnetic participates or pores. The stray field initiates the nucleation of reverse domains.

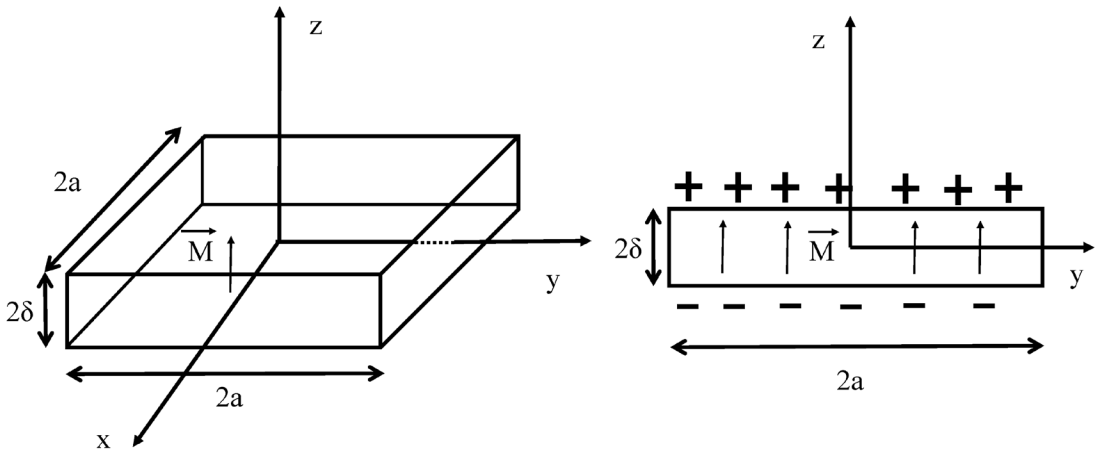

Figure 6-8 Sketch of a single platelet-shaped grain aligned along the z-axis and the cross-sectional image of the grain.

The integration over the surface of a platelet-shaped grain is complex. For simplicity, the stray field along the central z-axis (easy axis) will be estimated as follows. Instead of rectangular prism, a cylinder with dimensions $\pi r^2 \times 2\delta,\ (r = a)$ is used here (shown in Figure 6-9). The scalar potential is:

$$\begin{aligned}\Psi(0,0,z) &= \frac{1}{4\pi}\int M_S \frac{1}{\sqrt{x'^2+y'^2+(z-\delta)^2}}\cdot df' - \frac{1}{4\pi}\int M_S \frac{1}{\sqrt{x'^2+y'^2+(z+\delta)^2}}\cdot df'' \\ &= \frac{1}{4\pi}\int M_S \frac{2\pi r'dr'}{\sqrt{r'^2+(z-\delta)^2}} - \frac{1}{4\pi}\int M_S \frac{2\pi r''dr''}{\sqrt{r''^2+(z+\delta)^2}} \\ &= \frac{M_S}{2}\cdot(\sqrt{R^2+(z-\delta)^2} - \sqrt{(z-\delta)^2} - \sqrt{R^2+(z+\delta)^2} + \sqrt{(z+\delta)^2}) \\ &= \frac{M_S}{2}[\sqrt{R^2+(z-\delta)^2} - |z-\delta| - \sqrt{R^2+(z+\delta)^2} + |z+\delta|)\end{aligned}$$

(6.11)

And the stray field is:

$$\begin{aligned}\vec{H}_S(0,0,z) &= -\nabla\Psi = -\frac{\partial}{\partial z}(\frac{M_S}{2}[\sqrt{R^2+(z-\delta)^2} - |z-\delta| - \sqrt{R^2+(z+\delta)^2} + |z+\delta|)\cdot\hat{z} \\ &= -\frac{M_S}{2}[\frac{z-\delta}{\sqrt{R^2+(z-\delta)^2}} - \frac{z+\delta}{\sqrt{R^2+(z+\delta)^2}} + 2]\cdot\hat{z},\ |z| < \delta\end{aligned}$$

(6.12)

By substituting these parameters $r = 115nm,\ \delta = 45nm$ into Equation (6.12), Figure 6-10 shows the distribution of $\vec{H}_S(0,0,z)/\vec{M}_S$ along the central axis of the cylinder. The stray field increases slightly near the edge of the cylinder, which is in agreement with the simulation results done by Schmidts and his co-workers[45]. However, the stray field calculated based on Equation (6.12) only gives the information along the central axis and it cannot give the information about the stray field near the corner. The simulation model in the literature[45] shows that the stray field increase abruptly near the corners of grains and the torque caused by the stray field rotates the spontaneous magnetization out of its

easy axis even though there is no external magnetic field applied. This reversible rotation continues growing if a reverse external field is applied. However, the anisotropy field and exchange interaction will against this rotation. When the reverse external field is large enough, and overcome the anisotropy field and exchange interaction, the magnetization rotates to its reverse direction. Adding $Nd_{0.7}Cu_{0.3}$ alloy into the grain boundary phase has a large potential to round the corners of the grains and results in lower stray field, which is illustrated in Figure 6-11.

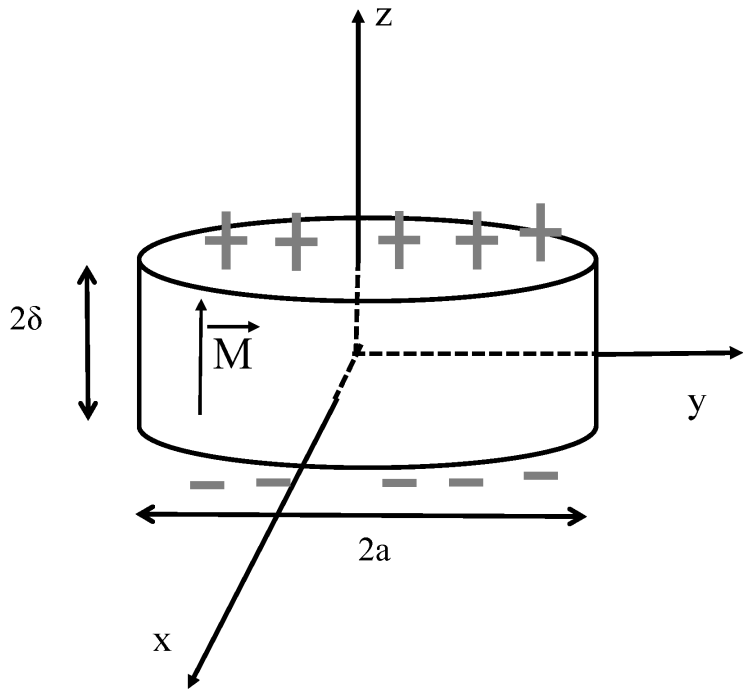

Figure 6-9 Sketch of a single cylindrical grain with dimensions of $\pi a^2 \times 2\delta$, aligned along the z-axis

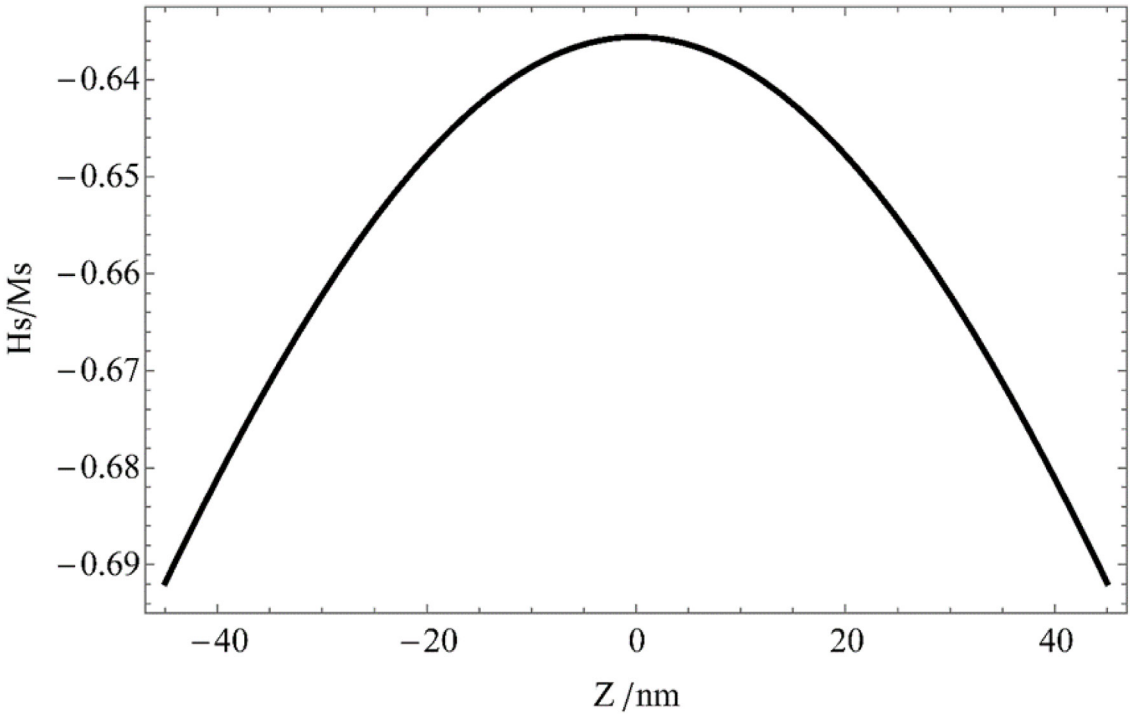

Figure 6-10 The distribution of Hs/Ms along the central axis of the cylindrical grain.

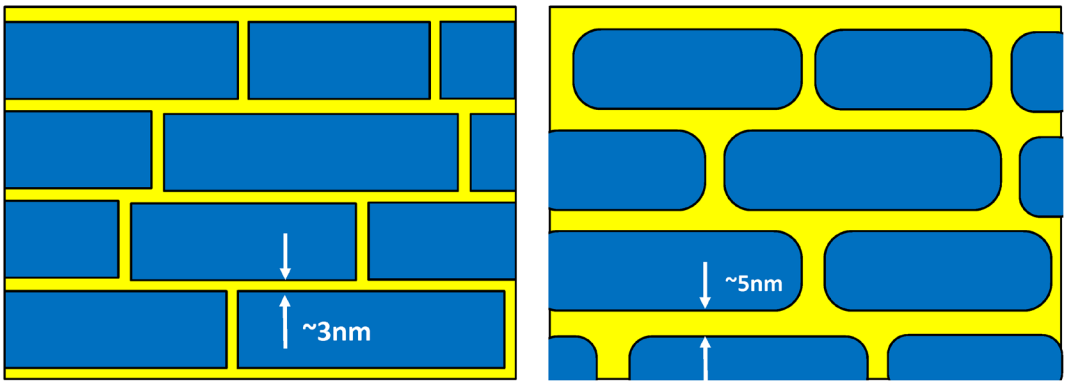

Figure 6-11 Adding $Nd_{0.7}Cu_{0.3}$ in the intergranular phase may decrease the stray field by rounding the corners of the grains.

Simulation result also shows[46, 47] that if the neighboring grains are magnetic isolated with each other by a nonmagnetic layer phase, then the effect of the nucleus of reverse domains on the neighboring grains can be suppressed. Diluting ~36% of the grain boundary phase by non-ferromagnetic $Nd_{0.7}Cu_{0.3}$ alloy may be not enough to magnetically segregate each of the grains. A simulation[48] for nanoscale permanent magnets ($d \approx 120nm$) considered the effect of grain boundary phase on the magnetic properties of materials. It shows that when the exchange constant A in the grain boundary region decreases, there is no significant changes in coercivity or in remanence; when the anisotropy constant K_1 in the grain boundary region decreases, the coercivity decreases; when the saturation magnetization M_S in the grain boundary region decreases, the coercivity increases and remanence slightly decreases. The third case is in agreement with our experimental data. Thus, the increase of coercivity in the hot-deformed magnets may be due to the decrease of M_S in the grain boundary region by adding non-ferromagnetic $Nd_{0.7}Cu_{0.3}$ additives. However, the causality between coercivity force and lower M_S in the grain boundary phase is not clear.

6.3 Conclusions

It is shown that the crystallographic alignment of hot-deformed magnets is not influenced by adding non-ferromagnetic $Nd_{0.7}Cu_{0.3}$ additives. The change in microstructure can result in magnets with sufficient coercivity that can satisfy the requirement for the traction motors used in the electric and hybrid vehicle but with lower amounts of Dy as compared to

commercially sintered magnets. Adding 5wt% $Nd_{0.7}Cu_{0.3}$ additives into the grain boundary region does not magnetically isolate the grains, but it does decrease the stray field near the corner of the grains.

Chapter 7

Summary

The hypothesis investigated in this work states that if bulk, rare-earth magnets are comprised of crystallographically-aligned, submicron Neodymium-Iron-Boron grains, separated from each other by a modified inter-granular phase, then each grain will only support a single magnetic domain and will be partially magnetically isolated from neighboring grains. This effect would cause the bulk magnet's coercivity to approach the maximum value possible for $Nd_2Fe_{14}B$. However, the experimental results have disproved this hypothesis. The conclusions drawn from each task are summarized as follows.

Quantitative expressions to predict the minimum amount of Dy needed for sintered magnets used in traction motors of electric and hybrid electric vehicles were developed. They show that the amount of Dy needed can be reduced from ~7wt% to ~4wt% if a post sintering Dy-diffusion treatment is implemented. The weight percent of Dy is the primary

indicator of high temperature coercivity, and the morphological variations in degree of magnetic alignment have a small to negligible impact on the high temperature resistance to demagnetization of these magnets.

Five hot-deformed magnets were manufactured at different temperatures (680°C, 750°C, 800°C, 850°C, 900°C) to analyze the effect of hot-deformation parameters on the microstructural and magnetic properties of magnets. The results show that the grain size increases and the stress decreases with an increase in hot-deformation temperature when the strain rate is kept constant. When the temperature reaches to 900°C, the grain size increases to $\sim 1100nm \times \sim 200nm$, which is large enough to support multiple domains in a single crystallite. It demonstrates that ~680°C is the optimal deformation temperature for manufacturing $Nd_2Fe_{14}B$-based magnets that are comprised of crystallographically-aligned submicron $Nd_2Fe_{14}B$ grains.

It also demonstrates that it is possible to fabricate bulk magnets that are comprised of crystallographically-aligned, submicron $Nd_2Fe_{14}B$ grains even though the inter-granular phase is diluted by non-magnetic $Nd_{0.7}Cu_{0.3}$ phase. The microstructure described above can result in magnets with sufficient coercivity to satisfy the requirement for traction motors used in the electric and hybrid vehicle while decreasing the amount of Dy required to ~2.5wt%. The change in inter-granular phase weakens the stray field but does not appear to magnetically isolate the grains. Adding 5wt% $Nd_{0.7}Cu_{0.3}$ additives into the grain boundary region may not be enough for magnetically isolation.

The work done in this research suggests that producing magnets with the hot-deformation process developed at MTU in order to reduce the amount of Dy required is potentially more cost-effective than using the Dy surface diffusion approach patented by Hitachi. Further investigation is required to determine both the mechanism by which the elevated temperature magnetic properties of $RE_2TM_{14}B$ magnets can be maintained with reduced Dy, and the extent to which this mechanism allows for the further reduction of Dy.

References

[1] K.C. P. Villars, Pearson's Crystal Data: Crystal Structure Database for Inorganic Compounds (on CD-ROM), Release 2013/14, ASM International®, Materials Park, Ohio, USA, (2013/14).

[2] J.F. Herbst, Rev. Mod. Phys., 63 (1991) 819-898.

[3] S. Hirosawa, K. Tokuhara, Y. Matsuura, H. Yamamoto, S. Fujimura, M. Sagawa, Journal of Magnetism and Magnetic Materials, 61 (1986) 363-369.

[4] M. Sagawa, S. Hirosawa, K. Tokuhara, H. Yamamoto, S. Fujimura, Y. Tsubokawa, R. Shimizu, Journal of Applied Physics, 61 (1987) 3559-3561.

[5] S. Hirosawa, Y. Matsuura, H. Yamamoto, S. Fujimura, M. Sagawa, H. Yamauchi, Jpn. J. Appl. Phys. Part 2 - Lett., 24 (1985) L803-L805.

[6] Y. Matsuura, S. Hirosawa, H. Yamamoto, S. Fujimura, M. Sagawa, Applied Physics Letters, 46 (1985) 308-310.

[7] M. Sagawa, S. Fujimura, H. Yamamoto, Y. Matsuura, K. Hiraga, IEEE Trans. Magn., 20 (1984) 1584-1589.

[8] R.K. Mishra, V. Panchanathan, J.J. Croat, Journal of applied physics, 73 (1993) 6470-6472.

[9] P.G. McCormick, W.F. Miao, P.A.I. Smith, J. Ding, R. Street, Journal of applied physics, 83 (1998) 6256-6261.

[10] H. Nakamura, K. Hirota, M. Shimao, T. Minowa, M. Honshima, IEEE Trans. Magn., 41 (2005) 3844-3846.

[11] R. Fischer, T. Schrefl, H. Kronmuller, J. Fidler, Journal of Magnetism and Magnetic Materials, 153 (1996) 35-49.

[12] M. Sagawa, S. Fujimura, Y. Yamamoto, Y. Matsuura, S. Hirosawa, K. Hiraga, Proceedings of the Eighth International Workshop on Rare-Earth Magnets and their Applications and the Fourth International Symposium on Magnetic Anisotropy and Coercivity in Rare Earth- Transition Metal Alloys, (1985) 587-611.

[13] J. Bauer, M. Seeger, H. Kronmuller, Journal of Magnetism and Magnetic Materials, 139 (1995) 323-334.

[14] R. Fischer, H. Kronmuller, Phys. Status Solidi A-Appl. Mat., 166 (1998) 489-511.

[15] A. Zern, M. Seeger, J. Bauer, H. Kronmuller, Journal of Magnetism and Magnetic Materials, 184 (1998) 89-94.

[16] H. Kronmuller, K.D. Durst, M. Sagawa, Journal of Magnetism and Magnetic Materials, 74 (1988) 291-302.

[17] H. Kronmuller, Phys. Status Solidi B-Basic Res., 144 (1987) 385-396.

[18] K. Hono, H. Sepehri-Amin, Scripta Materialia, 67 (2012) 530-535.

[19] R.W. Lee, Applied Physics Letters, 46 (1985) 790-791.

[20] L. Li, C.D. Graham, IEEE Trans. Magn., 28 (1992) 2130-2132.

[21] H.W. Kwon, J.H. Yu, IEEE Trans. Magn., 45 (2009) 4435-4438.

[22] W.B. Cui, Y.K. Takahashi, K. Hono, Acta Materialia, 59 (2011) 7768-7775.

[23] Y. Liu, Y. Ma, J. Li, C. Li, F. Xie, L. Chu, IEEE Trans. Magn., 46 (2010) 2566-2569.

[24] K.G. Knoch, B. Grieb, E.T. Henig, H. Kronmuller, G. Petzow, IEEE Trans. Magn., 26 (1990) 1951-1953.

[25] D.N. Brown, B. Smith, B.M. Ma, P. Campbell, IEEE Trans. Magn., 40 (2004) 2895-2897.

[26] K. Ohmori, L. Li, C.D. Graham, IEEE Trans. Magn., 28 (1992) 2139-2141.

[27] H. Sepehri-Amin, J. Liu, T. Ohkubo, K. Hioki, A. Hattori, K. Hono, Scripta Materialia, 69 (2013) 647-650.

[28] H. Sepehri-Amin, T. Ohkubo, T. Nishiuchi, S. Hirosawa, K. Hono, Scripta Materialia, 63 (2010) 1124-1127.

[29] T. Akiya, J. Liu, H. Sepehri-Amin, T. Ohkubo, K. Hioki, A. Hattori, K. Hono, Scripta Materialia, 81 (2014) 48-51.

[30] T. Akiya, J. Liu, H. Sepehri-Amin, T. Ohkubo, K. Hioki, A. Hattori, K. Hono, Journal of Applied Physics, 115 (2014).

[31] H. Sepehri-Amin, T. Ohkubo, K. Hono, Acta Materialia, 61 (2013) 1982-1990.

[32] W.C. Chang, T.B. Wu, K.S. Liu, Journal of Applied Physics, 63 (1988) 3531-3533.

[33] S.Z. Zhou, Y.X. Zhou, C.D. Graham, Journal of Applied Physics, 63 (1988) 3534-3536.

[34] T. Kawai, B.M. Ma, S.G. Sankar, W.E. Wallace, Journal of Applied Physics, 67 (1990) 4610-4612.

[35] P. Tenaud, A. Chamberod, F. Vanoni, Solid State Communications, 63 (1987) 303-305.

[36] G.P. Meisner, E.G. Brewer, Journal of Applied Physics, 72 (1992) 2659-2664.

[37] T.S. Chin, M.P. Hung, D.S. Tsai, K.F. Wu, W.C. Chang, Journal of Applied Physics, 64 (1988) 5531-5533.

[38] R. Zhao, W.C. Zhang, J.J. Li, H.J. Wang, M.G. Zhu, W. Li, Journal of Magnetics, 16 (2011) 294-299.

[39] Y. Yoshida, Y. Kasai, T. Watanabe, S. Shibata, V. Panchanathan, J.J. Croat, Journal of applied physics, 69 (1991) 5841-5843.

[40] L.F. Francis, Materials Processing: A Unified Approach to Processing of Metals, Ceramics and Polymers, Elsevier Science, 2015.

[41] H. Sepehri-Amin, T. Ohkubo, S. Nagashima, M. Yano, T. Shoji, A. Kato, T. Schrefl, K. Hono, Acta Materialia, 61 (2013) 6622-6634.

[42] K.D. Durst, H. Kronmuller, Journal of Magnetism and Magnetic Materials, 68 (1987) 63-75.

[43] S. Bance, B. Seebacher, T. Schrefl, L. Exl, M. Winklhofer, G. Hrkac, G. Zimanyi, T. Shoji, M. Yano, N. Sakuma, M. Ito, A. Kato, A. Manabe, Journal of Applied Physics, 116 (2014).

[44] D. Goll, M. Seeger, H. Kronmuller, Journal of Magnetism and Magnetic Materials, 185 (1998) 49-60.

[45] H.F. Schmidts, H. Kronmuller, Journal of Magnetism and Magnetic Materials, 94 (1991) 220-234.

[46] T. Schrefl, J. Fidler, H. Kronmuller, Journal of Magnetism and Magnetic Materials, 138 (1994) 15-30.

[47] T. Schrefl, H.F. Schmidts, J. Fidler, H. Kronmuller, Journal of Magnetism and Magnetic Materials, 124 (1993) 251-261.

[48] R. Fischer, H. Kronmuller, Phys. Rev. B, 54 (1996) 7284-7294.